The effects of cosmic rays on the formation of Milky Way-mass galaxies in a cosmological context

Tobias Buck [1]★ Christoph Pfrommer [1] Rüdiger Pakmor [2] Robert J. J. Grand [2] and Volker Springel [2]

[1] *Leibniz-Institut für Astrophysik Potsdam (AIP), An der Sternwarte 16, D-14482 Potsdam, Germany*
[2] *Max-Planck-Institut für Astrophysik, Karl-Schwarzschild-Str. 1, D-85748 Garching, Germany*

ABSTRACT

We investigate the impact of cosmic rays (CRs) and different modes of CR transport on the properties of Milky Way-mass galaxies in cosmological magnetohydrodynamical simulations in the context of the AURIGA project. We systematically study how advection, anisotropic diffusion, and additional Alfvén-wave cooling affect the galactic disc and the circumgalactic medium (CGM). Global properties such as stellar mass and star formation rate vary little between simulations with and without various CR transport physics, whereas structural properties such as disc sizes, CGM densities, or temperatures can be strongly affected. In our simulations, CRs affect the accretion of gas on to galaxies by modifying the CGM flow structure. This alters the angular momentum distribution that manifests itself as a difference in stellar and gaseous disc size. The strength of this effect depends on the CR transport model: CR advection results in the most compact discs while the Alfvén-wave model resembles more the AURIGA model. The advection and diffusion models exhibit large ($r \sim 50\,\mathrm{kpc}$) CR pressure-dominated gas haloes causing a smoother and partly cooler CGM. The additional CR pressure smoothes small-scale density peaks and compensates for the missing thermal pressure support at lower CGM temperatures. In contrast, the Alfvén-wave model is only CR pressure dominated at the disc–halo interface and only in this model the gamma-ray emission from hadronic interactions agrees with observations. In contrast to previous findings, we conclude that details of CR transport are critical for accurately predicting the impact of CR feedback on galaxy formation.

Key words: MHD – methods: numerical – cosmic rays – galaxies: evolution – galaxies: formation – galaxies: structure.

1 INTRODUCTION

The formation of galaxies is a multiscale, multiphysics problem and understanding the details of the physical processes involved is one of the most challenging problems in theoretical astrophysics. Cosmological simulations and semi-analytic studies have demonstrated that feedback from stellar winds and radiation fields, supernovae, and active galactic nuclei (AGNs) are key processes in shaping the structure of galaxies (e.g. Brook et al. 2012; Puchwein & Springel 2013; Stinson et al. 2013; Marinacci, Pakmor & Springel 2014; Vogelsberger et al. 2014; Henriques et al. 2015; Schaye et al. 2015; Dubois et al. 2016; Kaviraj et al. 2017; Hopkins et al. 2018; Pillepich et al. 2018). These processes effectively drive galactic winds, move gas and metals out of galaxies into the intergalactic medium, regulate the star formation rate (SFR) down to the observed low rates or completely quench it in elliptical galaxies, and balance radiative cooling in the centres of galaxy clusters (Kravtsov & Borgani 2012; Battaglia et al. 2012a,b, 2013; McCarthy et al. 2014, 2017; Dolag, Komatsu & Sunyaev 2016; Weinberger et al. 2017).

While the latest galaxy formation models are quite successful in reproducing key observables of realistic galaxies (e.g. Wang et al. 2015; Sawala et al. 2016; Grand et al. 2017; Hopkins et al.

2018; Buck et al. 2020), most feedback prescriptions are modelled empirically, calibrated against observed scaling relations which limits the predictive power of the corresponding calculations. In particular, resolution requirements of hydrodynamical simulations of galaxy formation made it necessary to implement feedback relatively coarsely: simulations base their feedback prescriptions on explicit sub-grid formulations which model the unresolved, multiphase structure of the interstellar medium (ISM; Springel & Hernquist 2003; Schaye & Dalla Vecchia 2008). The details of the driving mechanisms behind galactic winds and outflows are still unknown and implementations remain phenomenological (Oppenheimer & Davé 2006). On larger scales, feedback from AGNs has been invoked in order to balance star formation in galaxy clusters. Here, accretion rates on to the black hole are estimated by the Bondi prescription and feedback energy is injected in form of pure thermal energy (Di Matteo, Springel & Hernquist 2005; Springel et al. 2005) or they involve chaotic cold accretion (Gaspari, Ruszkowski & Oh 2013) or AGN feedback might be modelled slightly more complex (Weinberger et al. 2017; Davé et al. 2019).

Another obvious source of galactic feedback might be due to the energy and momentum deposition of the ultraviolet radiation of the stars. Radiation pressure acting on dust grains and the atomic lines in dense gas has been argued to transfer enough momentum to the gas in order to exceed the escape velocity and drive winds (Murray, Quataert & Thompson 2005; Thompson, Quataert & Murray 2005). However,

★ E-mail: tbuck@aip.de

direct radiation-hydrodynamical simulations in simplified set-ups (Krumholz & Thompson 2012) or in isolated galaxy simulations (Rosdahl et al. 2015) do not produce strong radiation pressure-driven winds, suggesting that radiation feedback is less effective and more gentle than widely assumed (but see also Emerick, Bryan & Mac Low 2018).

On the other hand, cosmological simulations often neglect feedback from relativistic particles, so-called CRs, which provide another source of non-thermal feedback. Such a particle population can be created by diffusive shock acceleration at expanding supernova remnants (e.g. Blandford & Eichler 1987; Jubelgas et al. 2008) or in AGN-powered jets (e.g. Sijacki et al. 2008; Ehlert et al. 2018). CRs and magnetic fields are observed to be in pressure equilibrium with the turbulence in the mid-plane of the Milky Way (Boulares & Cox 1990) and the pressure forces of the CRs might be able to accelerate the ISM and drive powerful galactic outflows as suggested by a number of theoretical works (Ipavich 1975; Breitschwerdt, McKenzie & Voelk 1991; Zirakashvili et al. 1996; Ptuskin et al. 1997; Breitschwerdt, Dogiel & Völk 2002; Everett et al. 2008; Socrates, Davis & Ramirez-Ruiz 2008; Samui, Subramanian & Srianand 2010; Dorfi & Breitschwerdt 2012) and local three-dimensional (3D) simulations of the ISM (Hanasz et al. 2013; Girichidis et al. 2016; Simpson et al. 2016).

In comparison to other feedback mechanisms, CRs have a number of advantageous properties: (i) the CR pressure drops less quickly upon adiabatic expansion than the thermal pressure due to their softer equation of state ($P_{CR} \propto \rho^{\gamma_{CR}}$ with $\gamma_{CR} = 4/3$), (ii) CR cooling is generally less efficient than the radiative cooling of a thermal plasma (Enßlin et al. 2007) and thus acts on longer time-scales compared to thermal energy, (iii) the non-thermal energy of CRs is not detectable through thermal observables or X-ray emission, therefore the (temporary) storage of feedback energy in CRs also avoids problems with the overproduction of these observables, (iv) they can maintain the outflows in a warm/hot state because the resonant production of Alfvén waves through the streaming instability (Kulsrud & Pearce 1969), and the dissipation of wave energy with various plasma physical wave damping processes energizes galactic winds as they rise in the galactic haloes.

A number of works have implemented CRs into 3D hydrodynamic simulations of galaxy formation and have demonstrated the ability of CRs to drive winds and regulate star formation (Jubelgas et al. 2008; Uhlig et al. 2012; Booth et al. 2013; Salem & Bryan 2014; Pakmor et al. 2016c; Pfrommer et al. 2017b; Ruszkowski, Yang & Zweibel 2017a; Jacob et al. 2018; Chan et al. 2019). CRs do not couple to the thermal gas via particle–particle collisions but via particle–wave interactions as fast streaming CRs along the magnetic field resonantly excite Alfvén waves. CRs are then able to scatter off of these waves which isotropise their distribution function in the wave frame, thus transferring energy and momentum to the thermal plasma and exerting a pressure on to the gas. Thereby, CRs not only impart momentum to the ISM at the launching sites but also continuously re-power winds via thermal and dynamic coupling of plasma and CRs.

As a result CRs might explain the observed low SFRs in giant elliptical galaxies located at the centres of galaxy groups and clusters. In the absence of any heating processes, the hot gaseous atmosphere of these objects is expected to efficiently cool and form stars at very high rates (up to a few hundred $M_\odot yr^{-1}$, e.g. Peterson & Fabian 2006). However, observed SFRs are much below these expected rates which is why AGN feedback has been invoked to balance radiative cooling. While theoretical considerations have shown that AGN feedback energies are sufficient, the exact coupling mechanism is still under debate (McNamara & Nulsen 2007). While several physical

processes have been proposed to mediate the heating (amongst others the dissipation of turbulent energy powered by the AGN, Zhuravleva et al. 2014) a promising alternative is given by CRs. A net outward flux of streaming CRs can resonantly excite Alfvén waves that experience non-linear Landau damping or decay via a cascading process as a result of strong external turbulence and eventually dissipate locally (Loewenstein, Zweibel & Begelman 1991; Guo & Oh 2008; Enßlin et al. 2011; Pfrommer 2013; Wiener, Oh & Guo 2013; Jacob & Pfrommer 2017a,b; Ruszkowski, Yang & Reynolds 2017b; Ehlert et al. 2018).

By now there are several (magneto-)hydrodynamics (MHD) simulation codes capable of solving the details of the CR proton acceleration and transport in galaxies and galaxy clusters: the Eulerian mesh codes COSMOCR (Miniati et al. 2001), ZEUS-3D (Hanasz & Lesch 2003), the smoothed particle hydrodynamics code GADGET-2 (Pfrommer et al. 2006; Enßlin et al. 2007; Jubelgas et al. 2008), the adaptive mesh refinement codes RAMSES (Booth et al. 2013; Dubois et al. 2016), ENZO (Salem & Bryan 2014), FLASH (Girichidis et al. 2016), and PLUTO (Mignone et al. 2018), the moving-mesh code AREPO (Pakmor et al. 2016b; Pfrommer et al. 2017a) and the mesh-free Lagrangian finite mass code GIZMO (Chan et al. 2019). Here, we use the AREPO code (Springel 2010; Pakmor et al. 2016a) combined with the numerical implementations of CR physics (Pakmor et al. 2016b; Pfrommer et al. 2017a) to simulate the formation of Milky Way (MW) like galaxies in a cosmological context.

This paper is organized as follows: In Section 2, we describe the simulation setup and the different implementations of CR treatment. In Section 3, we study the central stellar and gaseous discs focussing on the differences and similarities in properties across various CR physics variants. We further investigate here the accretion of gas on to the main galaxy and the successive build-up of angular momentum. In Section 4, we turn to analyse the effects of CRs on the properties and structure of the CGM. We finish our analysis in Section 5 by comparing a direct observable, namely the gamma-ray luminosity of the simulated galaxies, to observations. In Section 6.3, we conclude this paper with a discussion, compare our results to previous work, and summarize our results in Section 7.

2 COSMOLOGICAL SIMULATIONS

For this work we simulate the formation of two MW-like disc galaxies from cosmological initial conditions taken from the AURIGA project (Grand et al. 2017, 2019). Simulations are performed with the second-order accurate, adaptive moving-mesh code AREPO (Springel 2010; Pakmor et al. 2016a) which includes important physical prescriptions to model galaxy formation in a cosmological setup. For completeness we describe the most important models below but refer the reader to the works of Grand et al. (2017) and Pakmor et al. (2016b) for more technical details on the AURIGA galaxy formation model and to Pfrommer et al. (2017a) for details on the CR physics.

The AURIGA model includes primordial and metal-line cooling with self-shielding corrections and the spatially uniform UV background model of Faucher-Giguère et al. (2009) is included (for more details see Vogelsberger et al. 2013). The ISM is modelled with an effective equation of state (Springel & Hernquist 2003) and star-forming gas is treated as a two phase medium. Star formation occurs in thermally unstable gas for densities higher than a threshold density of $n_{th} = 0.13\,cm^{-3}$ in a stochastic manner where the probability scales exponentially with time in units of the star formation time-scale ($t_{sf} = 2.2$ Gyr in the AURIGA model).

Each star particle in this model represents a single stellar population (SSP) characterized by age and metallicity assuming a Chabrier

(2003) initial mass function (IMF). The mass-loss and metal return of each star particle is calculated for supernovae of type II (SNII), SNIa, and AGB stars at each time step. The mass and metal yields are taken from Karakas (2010) for AGB stars, and Portinari, Chiosi & Bressan (1998) for core-collapse SNe. Mass and metals are distributed among nearby gas cells with a top-hat kernel. SNIa events are calculated using a delay time distribution function and their mass and metal return follows the yield tables from Thielemann et al. (2003) and Travaglio et al. (2004). The number of SNII is calculated from the number of stars in the mass range 8–100 $M_\odot$ and feedback is assumed to occur instantaneously. An active gas cell (star forming) is probabilistically chosen to either form a star particle or become a site for SNII events (see Vogelsberger et al. 2013) in which case a wind particle is launched in an isotropically random direction. The wind velocity is coupled to the one-dimensional velocity dispersion of the dark matter halo. The wind particle interacts only gravitationally until either a gas cell with a density below 0.05 times the threshold density for star formation is reached, or the maximum traveltime is exceeded. Meeting either of the criteria, the wind particle re-couples and deposits its mass, metals, momentum, and thermal energy into the gas cell in which it is located (see Grand et al. 2017, and references therein for more details). Note, CRs are directly injected into neighbouring cells of a supernova and as such wind particles neither transport CR energy nor the magnetic field.

AGNs feedback is implemented following Springel et al. (2005). The mass growth from gas accretion is described by Eddington-limited Bondi–Hoyle–Lyttleton accretion (Bondi & Hoyle 1944; Bondi 1952) in addition to a term that models the radio mode accretion (see Grand et al. 2017, for more details). Magnetic fields are treated with ideal MHD (Pakmor, Bauer & Springel 2011; Pakmor & Springel 2013) and are seeded at redshift $z = 127$ with a homogeneous magnetic field of 10^{-14} (comoving) Gauss. The divergence cleaning scheme of Powell et al. (1999) is implemented to ensure that the divergence of the magnetic field vanishes.

Finally, CRs are modelled as a relativistic fluid with a constant adiabatic index of 4/3 in a two-fluid approximation (Pfrommer et al. 2017a). CRs are generated at core-collapse supernovae remnants by instantaneously injecting all CR energy produced by the star particle into its surroundings immediately after birth. The energy efficiency of the injection is set to $\zeta_{SN} = 0.1$. Following Pfrommer et al. (2017a), we assume an equilibrium momentum distribution for the CRs to model their cooling via Coulomb and hadronic interaction with the ambient gas.

To bracket the uncertainties of CR transport, we simulate three different models with different variants of CR physics (similar to Wiener, Pfrommer & Oh 2017) and one model without CRs. To explain the differences of our CR models, we briefly review the main aspects of CR hydrodynamics. While individual CRs move close to the speed of light, frequent resonant CR interactions with Alfvén waves cause their distribution function to (nearly) isotropise in the frame of the Alfvén waves such that the CR energy is transported as a superposition of CR advection with the gas, anisotropic streaming with Alfvén waves along the magnetic field and diffusion with respect to the wave frame so that the time evolution equation of the CR energy density ε_{cr} in the one-moment formulation of CR transport reads as follows:

$$\frac{\partial \varepsilon_{cr}}{\partial t} + \nabla \cdot \left[\underbrace{\varepsilon_{cr} \boldsymbol{v}}_{\text{advection}} + \underbrace{(\varepsilon_{cr} + P_{cr})\boldsymbol{v}_{st}}_{\text{streaming}} - \underbrace{\kappa_\varepsilon \boldsymbol{b}(\boldsymbol{b} \cdot \nabla \varepsilon_{cr})}_{\text{anisotropic diffusion}} \right]$$
$$= - \underbrace{P_{cr} \nabla \cdot \boldsymbol{v}}_{\text{adiab. changes}} - \underbrace{|\boldsymbol{v}_A \cdot \nabla P_{cr}|}_{\text{Alfven cooling}} + \underbrace{\Lambda_{cr} + \Gamma_{cr}}_{\text{losses \& sources}} . \quad (1)$$

Here, $\boldsymbol{v}$ denotes the gas velocity, $\boldsymbol{v}_A = \boldsymbol{B}/\sqrt{4\pi\rho}$ is the Alfvén velocity, $\boldsymbol{B}$ is the magnetic field, ρ is the gas mass density, $\boldsymbol{v}_{st}$ is the CR streaming velocity,

$$\boldsymbol{v}_{st} = -\boldsymbol{v}_A \, \text{sgn}(\boldsymbol{B} \cdot \nabla P_{cr}) = -\frac{\boldsymbol{B}}{\sqrt{4\pi\rho}} \frac{\boldsymbol{B} \cdot \nabla P_{cr}}{|\boldsymbol{B} \cdot \nabla P_{cr}|}, \quad (2)$$

implying that the CR streaming velocity is oriented along magnetic fields lines down the CR pressure gradient with a velocity that corresponds in magnitude to $\boldsymbol{v}_A$, P_{cr} is the CR pressure, κ_ε is the kinetic energy-weighted spatial CR diffusion coefficient, $\boldsymbol{b} = \boldsymbol{B}/|\boldsymbol{B}|$ is the unit vector along the local magnetic field, and Λ_{cr} and Γ_{cr} are non-adiabatic CR losses and sources.

Note that CR streaming and diffusion are both anisotropic transport processes along the mean magnetic field and oriented down the CR gradient. While the streaming term advects CRs with the frame of Alfvén waves and maintains CR gradients, diffusion is a dispersive process (owing to the second gradient in the bracket of equation 1) so that the CR gradient weakens over time, implying that the streaming and diffusion fluxes cannot be the same at all times (Wiener et al. 2017). Most importantly, CR diffusion exactly conserves the CR energy while CR streaming drains CR energy at a rate $|\boldsymbol{v}_A \cdot \nabla P_{cr}|$ due to the excitation of resonant Alfvén waves.

In all of our models we omit the CR streaming term on the left-hand side of equation (1), which can be most accurately solved with the two-moment method of CR transport (Jiang & Oh 2018; Thomas & Pfrommer 2019). In all three CR models, we account for CR advection and adiabatic changes of the CR energy. Our models are defined as follows:

(i) **noCR**: fiducial AURIGA galaxy formation model without CRs.

(ii) **CRadv**: CR advection model where CRs are only advected with the gas.

(iii) **CRdiff**: CR diffusion model where CRs are advected with the gas but are further allowed to anisotropically diffuse relative to the rest frame of the gas with a diffusion coefficient of $\kappa_\parallel = 10^{28}$ cm^2 s^{-1} along the magnetic field and no diffusion perpendicular to it (Pakmor et al. 2016b).

(iv) **CRdiffalfven**: anisotropic CR diffusion model with the additional inclusion of the Alfvén-wave cooling term that arises due to the energy transfer from CRs to Alfvén waves that are self-excited through the resonant CR streaming instability (Kulsrud & Pearce 1969).

While CR diffusion is thought to describe the transport of high-energy CRs above $\sim$200 GeV, at lower energies the transport transitions to mainly CR streaming with self-generated Alfvén waves (Evoli et al. 2018), although the role of scattering in external turbulence is not yet settled (Zweibel 2017). While the process of CR diffusion conserves CR energy, additionally accounting for the Alfvén-wave cooling term emulates and approximates CR streaming. While this approximation is justified in cases for which the diffusion and streaming fluxes match each other, solutions will necessarily deviate if this condition is not fulfilled (Wiener et al. 2017). Future work is needed to clarify how the explicit inclusion of CR streaming in the presence of different wave damping processes changes the picture presented in this work.

3 GALAXY DISC PROPERTIES

3.1 Stellar disc

In Fig. 1, we present face-on and edge-on projections of all eight simulations at $z = 0$ where the upper panels show the four different
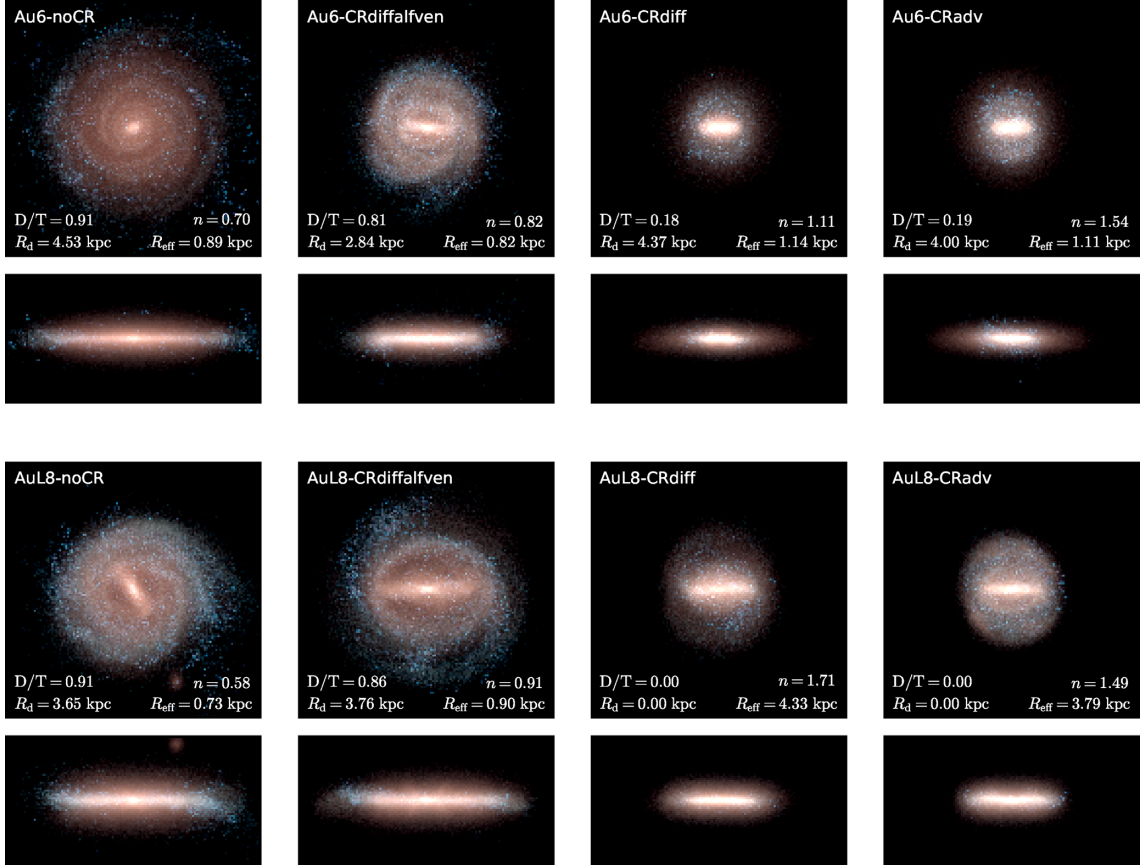
Figure 1. Face-on and edge-on projected stellar density at $z = 0$ for the eight simulations. The upper panel shows the galaxy Au6 and the lower panel shows AuL8. From left to right we show the four different variants of physics: (i) the fiducial AURIGA simulations without CRs, (ii) the simulations with CR advection and anisotropic CR diffusion and Alfvén cooling/heating enabled, (iii) the CR anisotropic diffusion and CR advection simulations, and (iv) the pure CR advection simulations. The images are synthesized from a projection of the K-, B- and U-band luminosity of stars, which are shown by the red, green and blue colour channels, in logarithmic intervals, respectively. Younger (older) star particles are therefore represented by bluer (redder) colours. In each face-on panel we note structural properties of the stellar disc resulting from a surface density fit of a combined exponential plus Sérsic (1963) profile (see Fig. A1). The plot dimensions are 50 kpc × 50 kpc and 50 kpc × 25 kpc, respectively.

simulations of the Au6 halo and lower panels of AuL8. The images are a composition of the K-, B- and U-band luminosities (mapped to the red, green, and blue colour channels), which indicate the distribution of younger (bluer colours) and older (redder colours) star particles, respectively. All simulations reveal a star-forming disc component with additional clear non-axisymmetric structures such as bars and spiral arms. For the fiducial noCR and the CRdiffalfven model the stellar disc is radially extended and thin. In contrast to that, the CRdiff and CRadv models result in more compact stellar discs further indicated by the lower ratio of D/T between the stellar disc mass (D) and the total stellar mass of the galaxy (T) shown in the lower right corner of each panel. Nevertheless, from the edge-on view these simulations are still identifiable as disc galaxies.

Despite the obvious differences in morphology, the total stellar mass in each model is almost the same as shown by Fig. 2. Here, we investigate the star formation history (SFH) and the stellar mass–halo mass relation of the galaxies in the four different models. The SFH of halo Au6 is shown in the left most panel, the one of halo AuL8 in the middle panel and the right-hand panel shows the stellar mass as function of the halo mass in comparison to abundance matching results from Moster et al. (2013). Within their intrinsic scatter, the SFHs of each physics run do not differ much and the total stellar mass of each galaxy varies only within a factor of $\lesssim 1.5$ at the end of each

run (see also Table 1). For halo AuL8, we find that the CRs slightly suppress the stellar mass growth already at early times ($z \sim 2$) as can be appreciated from the suppressed SFR (middle panel). At redshift zero the CRdiffalfven run has very similar stellar mass compared to the AURIGA run caused by a late time ($z \lesssim 0.2$) burst in star formation (see red line in the middle panel) whereas the CRdiff and CRadv run have slightly lower stellar mass. Halo Au6 on the other hand acquires slightly more stellar mass in the CR runs compared to the fiducial AURIGA model, at late times ($z < 0.5$) also visible in the enhanced late time SFR (left-hand panel of Fig. 2) for the CR runs.

We further examined the total amount of gas as well as the cold gas mass and found that both quantities do not change much across the different physics variants. We conclude that in our simulations structural disc properties can be significantly changed by CRs, global stellar properties, however, are robust across different CR physics variants and are not much affected by CRs.

3.2 Gas disc

The differences in stellar morphology are mainly a result of differences in the gaseous properties of the central galaxies. Fig. 3 shows face-on and edge-on projections of the gas surface density (upper
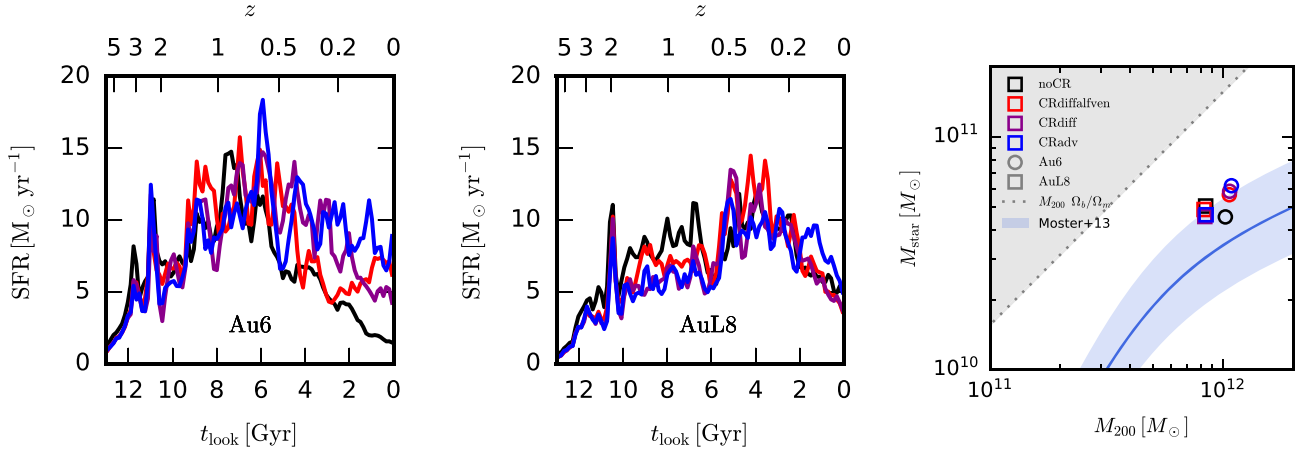
Figure 2. SFHs and the stellar mass–halo mass relation (right-hand panel) for the AURIGA haloes. We show the SFHs for galaxy Au6 (left-hand panel) and for AuL8 (middle panel), respectively. In the right-hand panel, we show the final stellar mass of our simulations at $z = 0$ versus their final halo mass. In each panel, we compare the SFH/stellar masses of the four different physics variants, the fiducial Auriga model shown in black, the CR advection run in blue, the run with additional anisotropic CR diffusion in purple, and the run which additionally accounts for CR Alfvén wave cooling in red. In the right-hand panel, the light blue line shows the abundance matching result taken from Moster, Naab & White (2013) while the grey dotted line shows the cosmic baryon fraction.

Table 1. Properties of the main galaxies: We state the virial mass, M_{200}, virial radius, R_{200}, the stellar mass, M_{star}, and the gas mass, M_{gas}, as well as the disc and bulge masses, M_d, M_b, as resulting from a combined exponential plus Sérsic (1963) fit to the azimuthally averaged surface density profile. We further report the disc scale length, R_d, the bulge effective radius, R_{eff}, the bulge sersic index, n, and the disc-to-total ratio D/T of that fit.

Simulation	M_{200} $(10^{12}\,M_\odot)$	R_{200} (kpc)	M_{star} $(10^{10}\,M_\odot)$	M_{gas} $(10^{10}\,M_\odot)$	M_d $(10^{10}\,M_\odot)$	R_d (kpc)	M_b $(10^{10}\,M_\odot)$	R_{eff} (kpc)	n	D/T
				Auriga-6 (Au6)						
noCR	1.02	212.39	4.36	7.88	4.17	4.53	0.41	0.89	0.69	0.91
CRdiffalfven	1.06	215.18	5.54	9.12	4.37	2.84	1.03	0.82	0.83	0.81
CRdiff	1.07	215.43	5.81	8.91	1.03	4.37	4.64	1.14	1.11	0.18
CRadv	1.09	216.71	6.19	9.47	1.11	4.00	4.79	1.11	1.54	0.19
				Auriga-L8 (AuL8)						
noCR	0.84	199.02	4.82	7.00	4.39	3.65	0.41	0.73	0.58	0.91
CRdiffalfven	0.83	197.96	4.72	6.06	4.08	3.76	0.67	0.90	0.91	0.86
CRdiff	0.83	198.48	4.51	6.65	0.00	0.00	4.51	4.33	1.71	0.00
CRadv	0.85	199.33	4.58	7.76	0.00	0.00	4.58	3.79	1.49	0.00

panels), the magnetic field strength (middle panels), and the ratio of CR-to-thermal pressure, X_{cr}, (lower panels) of the central gaseous disc of Au6. From left to right we show the noCR, the CRdiffalfven, the CRdiff, and the CRadv run. The magnetic field is calculated as $B = \sqrt{\langle B^2 \rangle_V}$ and the value of X_{cr} is calculated as the ratio of volume-weighted pressure terms, $X_{cr} = \langle P_{cr}\rangle_V/\langle P_{th}\rangle_V$. Fig. 4 complements this by showing the radial profiles in cylindrical bins of radial width 1 kpc and height ± 3 kpc centred on the disc mid-plane for both galaxies Au6 (upper panels) and AuL8 (lower panels). The profiles have been obtained by adding up thermodynamic extensive quantities. This means, that we have volume-weighted (energy-)densities within a given concentric shell, while temperature averages are calculated via mass weighting.

Comparing the surface density maps of the four different physics variants we find that the CR runs show a more centrally concentrated, thicker gas disc with slightly higher surface densities within the disc region. This is further highlighted by the larger central densities in the left-hand panels of Fig. 4. Furthermore, from Fig. 3 we see how the CR pressure smoothes out density features in the disc, particularly in the CRadv and CRdiff runs; the CRdiffalfven run most closely resembles the fiducial AURIGA run. The CRadv run exhibits the most compact, thick, and smooth gas disc where the

additional CR pressure stabilizes and smoothes the gas. The lower panels of Fig. 3 and the third panels from the left of Fig. 4 show that in all three CR models the thermal pressure in the gas disc is sub-dominant in comparison to the CR pressure. This effect is most prominent in the CRadv and CRdiff runs where CRs can only cool adiabatically via Coulomb and hadronic interactions. This results in CR-to-thermal pressure ratios of $P_{cr}/P_{th} = X_{cr} \gtrsim 10$ in the disc region.

We observe slightly higher CR-to-thermal pressure ratios in the CRdiff compared to the CRadv run. At first, this result might be surprising because the CRs in the diffusion run are able to diffuse out of the disc into the halo. The reason for this is as follows: if $|\nabla(P_{cr} + P_{th})| > |\rho\nabla\Phi|$ (where P_{th} is the thermal pressure and Φ is the gravitational potential), then the composite of CRs and thermal gas adiabatically expands and as a result the CR pressure will exceed the thermal pressure because of its softer equation of state; the CR pressure decreases at a slower rate in comparison to the thermal pressure. As the CRs diffuse above and below the galaxy mid-plane, they push gas out of the disc (via their gradient pressure force), thus lowering the gas density in the disc (see left-hand panels of Fig. B1). Because the temperature in the star-forming regions is set by the effective equation of state, the thermal pressure in the CRdiff model
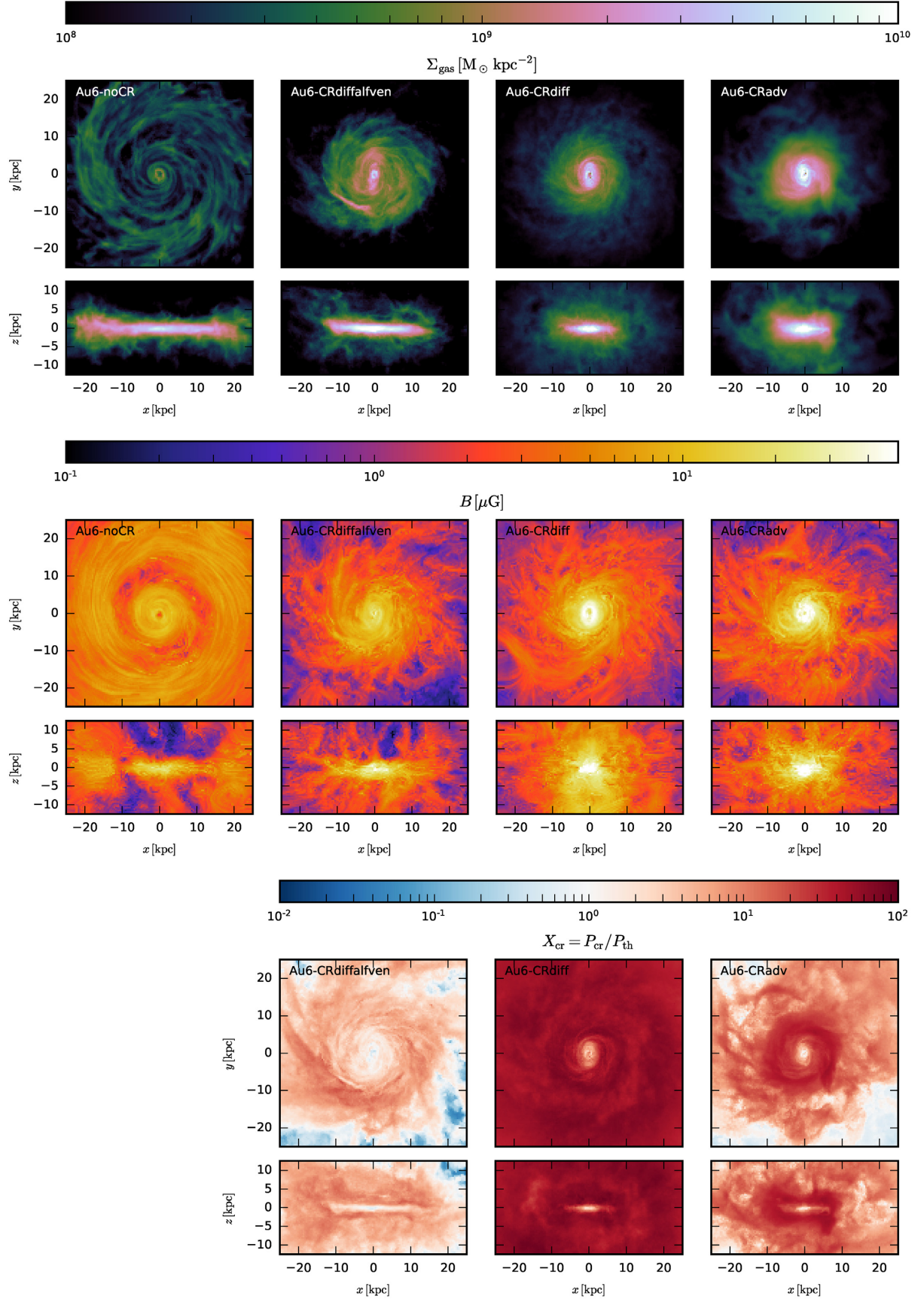
Figure 3. From top to bottom we show the gas surface density, the volume-weighted magnetic field strength, $\sqrt{\langle B^2 \rangle_V}$, and the CR-to-thermal pressure ratio, $X_{\mathrm{cr}} = \langle P_{\mathrm{cr}} \rangle_V / \langle P_{\mathrm{th}} \rangle_V$, of the different physics variants (left to right) in the Au6 simulation in face-on and edge-on projections. The projection depth is 25 kpc.
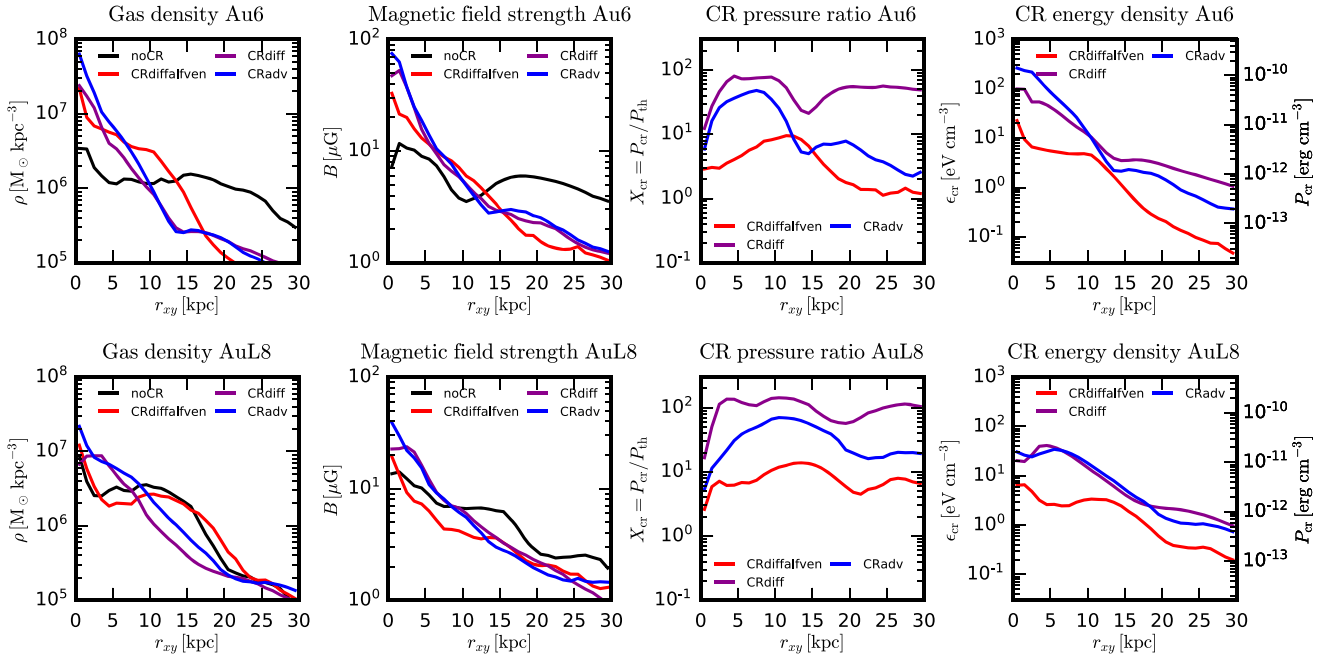
Figure 4. Radial profiles of gas density, magnetic field strength, CR-to-thermal pressure ratio, and CR pressure and energy density (left to right) in cylindrical shells of height $|z| = 3$ kpc and width $\Delta r_{xy} = 1$ kpc. The upper panels show results for the model galaxy Au6 and lower panels for AuL8. Different physics variants are shown with differently coloured lines. The fiducial AURIGA run is shown with a black line, the Alfvén run in red, the CR diffusion run in magenta and the CR advection run in blue.

is lower (see right most panels of Fig. B1), and hence the ratio of $P_{cr}/P_{th} = X_{cr}$ is larger in this model.

In the CRdiffalfven run on the other hand, the CRs are allowed to diffuse and to cool via the Alfvén wave cooling mechanism and thus their stabilizing pressure is less dominant compared to the CRadv run. Here, we find typical values of X_{cr} ranging from three to ten within the central 5–10 kpc of the disc (see Fig. 4). This allows for a shallower radial density profile within the disc that is then able to grow larger stellar discs. The right-most panel of Fig. 4 shows the radial profiles of the disc CR pressure and the energy density, respectively, averaged over a height of $|z| = 3$ kpc. The CR energy density is decreasing with radius and follows in general the shape of the gas density profile with breaks at $r_{xy} \sim 14$ kpc and 20 kpc for Au6 and AuL8, respectively. At the solar radius (~ 8 kpc) the value of the CR energy density is $\epsilon_{cr} \sim 4$–5 eV cm^{-3} for Au6 ($\epsilon_{cr} \sim 2$ eV cm^{-3} for AuL8) in the CRdiffalfven model while the other two models show a factor of $\gtrsim 3$ higher values. A more detailed comparison to observations follows in Section 6.1. We caution that some of the drastic differences of the density profiles between the different variants of CR physics may be due to cosmic variance and the different accretion histories. In particular the differing density profiles in Au6 (Fig. 4) are reduced in AuL8 where the CRdiffalfven run's density profile follows much more closely the fiducial AURIGA run.

The middle panel of Fig. 3 shows the magnetic field strength which looks very similar in the disc for all CR runs but varies drastically from the fiducial AURIGA runs which show a much smoother, ordered magnetic field. Looking at the second panels of Fig. 4 we find that the magnetic field strength at the edge of the stellar disc (~ 20 kpc) is around 1.5 to 2.5 μG (except for the fiducial Au6 run which shows values of ~ 6 μG). The magnetic field strength in our models increases towards the central regions of the disc. In the inner disc (at radii of $\lesssim 5$ kpc) we find magnetic field strengths of $\gtrsim 7$–15 G ($\gtrsim 9$–20 μG for Au6) depending on the CR model at hand.

These values of the magnetic field strength are in good agreement with estimates for the MW (Haverkorn et al. 2006; Sun & Reich 2012; Haverkorn 2015; Pakmor et al. 2018) and local disc galaxies (Beck et al. 2019). In detail, the CR runs show a more structured magnetic field which follows closely the structure of the gas disc because the CRs act as a local feedback source while in the noCR run the wind feedback is non local. Thus, CRs are able to inject turbulence in the gas disc, imprinting more small-scale structure on to the magnetic field. This feature is absent in the noCR runs and thus the magnetic field appears much more ordered. However, the halo magnetic field looks very different between the three CR runs. Interestingly, the vertical magnetic field extending into the halo in the CRdiff and CRadv is larger compared to the CRdiffalfven and AURIGA runs. Thus, we conclude that CR dynamics alters the dynamo process in comparison to pure MHD simulations and the higher density features in the CR runs lead to a more structured magnetic field in the gas disc (see also middle panels of Fig. 4). We note that different variants of CR transport seem not to affect the disc magnetic field much.

3.3 Gas accretion on to the disc

We have seen that the inclusion of CRs lead to more compact stellar and gaseous discs. In this section, we investigate the evolution of the angular momentum of gas that ends up in stars in the central galaxy at present day. In practice, we make use of Lagrangian 'tracer particles' (Genel et al. 2013; Grand et al. 2019) to follow the motion of resolution elements over time. At the beginning of each simulation, each gas cell in the high-resolution region is assigned a tracer particle with a unique ID. A tracer particle in any given cell moves to a neighbouring cell with a probability proportional to the outward mass flux across a cell face. Usually, a tracer particle has the highest probability to remain in the same cell, because the moving-mesh
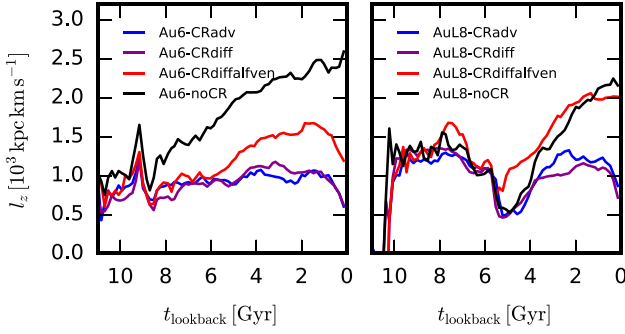
Figure 5. Median specific angular momentum evolution of the gas that ends up in the stellar disc at redshift $z = 0$. Au6 is shown in the left-hand panel and AuL8 in the right. At lookback times of $t_{lookback} \sim 6$ Gyr AuL8 is undergoing a major merger causing the dip in the angular momentum evolution.

nature of AREPO means that cells follow the bulk gas flow as closely as possible.

Following the median angular momentum of gas which is in stars at redshift $z = 0$ back in time (Fig. 5) we find that CRs suppress the acquisition of angular momentum after the time of disc formation ($t_{lookback} \sim 5$–8 Gyr). The suppression is strongest for the CRadv and CRdiff runs while the CRdiffalfven run more closely follows the fiducial runs. At present day, the CR simulations have acquired a factor of $\sim$2–5 times less specific angular momentum which manifests itself in more compact discs. For AuL8, the differences between the noCR run and the CR runs are smaller and the CRdiffalfven run matches the angular momentum of the noCR run. At a lookback time of 6 Gyr this galaxy undergoes a merger which masks most of the differences in angular momentum distribution between the different physics runs. The evolution of the median angular momentum is indeed representative of the evolution of the entire distribution of gas angular momentum, as can be verified in Fig. C1.

The angular momentum acquisition of the galaxy is most efficient if the accreted gas from large scales is undisturbed and flows to the central gas disc. When a large gas disc is first forming in the fiducial AURIGA model the wind feedback model develops outflows perpendicular to the stellar/gas disc (e.g. left-hand panel in Fig. 6),

which is an emergent phenomenon that is the result of the outflow taking the path of least resistance away from the galaxy (Grand et al. 2019). As we have discussed earlier (Fig. 3), in the CR runs the additional CR pressure support inflates the gas disc and thus enhances the gas density above and below the disc. The gas morphology in these runs is thus less discy and the particular implementation of the wind model results in more spherically symmetric gas flows that are less coherent in the perpendicular direction of the disc as we exemplify in Fig. 6. This figure shows the gas flow pattern in form of stream lines at redshift $z = 0.3$ (corresponding to a lookback time of $\sim$3.5 Gyr).

In order to compare the wind properties to the dominant pressure forces and assess whether CRs change the hydrodynamic halo properties, we overlay the streamlines of Fig. 6 on a colour map that shows the pressure ratio $(P_{cr} + P_{th})/P_{kin, r}$, where $P_{kin, r} = \rho v_r^2$ is the radial kinetic flux term in the Euler equation. This can be seen by looking at the momentum equation of an ideal fluid in the presence of CRs, which reads as follows:

$$\frac{\partial \rho \boldsymbol{v}}{\partial t} + \nabla \cdot (\rho \boldsymbol{v} \boldsymbol{v}^{\mathrm{T}} + P \boldsymbol{1} - \boldsymbol{B} \boldsymbol{B}^{\mathrm{T}}) = -\rho \nabla \Phi, \qquad (3)$$

where $P = P_{cr} + P_{th} + P_{mag}$ and $\boldsymbol{1}$ is the unit rank-two tensor. Converting this equation to spherical coordinates and neglecting the pressure and tension term of subdominant magnetic fields, the radial momentum flux density is given by $\rho v_r^2 + P_{cr} + P_{th}$ (Mihalas & Mihalas 1984). Fig. 6 shows that the divergence in the stream lines ($\nabla \cdot \boldsymbol{v} < 0$) corresponds to a shock where kinetic energy is converted into thermal energy.

The noCR simulation in Fig. 6 shows coherent outflows along the direction of the spin axis of the disc, which enable flow channels to open up in the perpendicular direction along which low-metallicity gas can be coherently accreted to the central disc (Pakmor et al. in preparation). Whereas the gas flow in the CRdiffalfven run more closely resembles the flow pattern of the fiducial AURIGA model, the direction of the outflows is less ordered and not always perpendicular to the disc. The CRdiff and CRadv runs on the other hand show more spherical, slower outflows which shock the inflowing gas at a distance of $r \sim 100$–200 kpc, shutting off the coherent gas inflows to the central galaxy while at the same time preventing coherent outflows to large distances. Therefore, these models exhibit a more
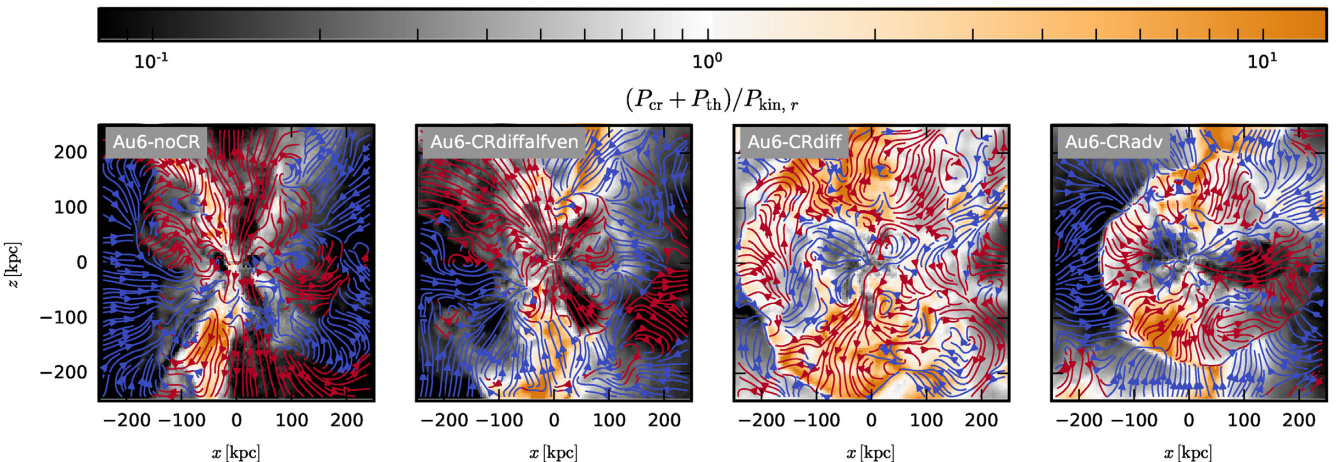

Figure 6. CGM gas flow patterns of the halo Au6 at redshift $z = 0.3$ where the stellar disc is shown edge-on. Streamlines indicate the direction of gas flow and arrow colours indicate the sign of the radial velocity of the flow. Red colours signal outflowing gas and blue colours in-flowing gas, respectively. The thickness of the gas slice is 20 kpc in the y-direction and the background colour coding shows the pressure ratio $(P_{cr} + P_{th})/P_{kin, r}$, i.e. the sum of CR and thermal pressure over the radial kinetic flux term in the Euler equation, $P_{kin, r} = \rho v_r^2$.
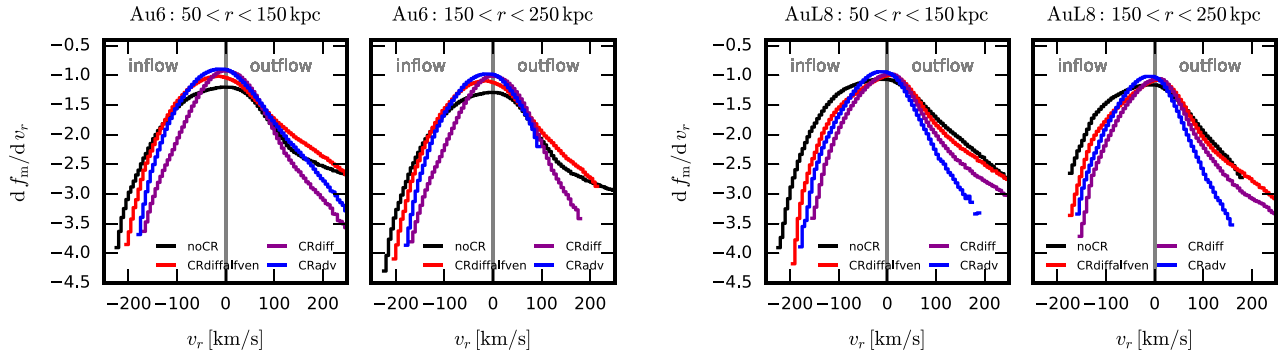
Figure 7. Time averaged mass weighted distribution of the gas radial velocity in two different 100 kpc wide spherical shells for the Au6 halo in the two left most panels and the Au8 halo in the two right most panels. The CR runs show a suppressed tail towards large inflow velocities in comparison to the noCR runs. Time averaging is done for 10 snapshots in the redshift range $0.2 < z < 0.3$ corresponding to a time span of $t \sim 1.3$ Gyr.
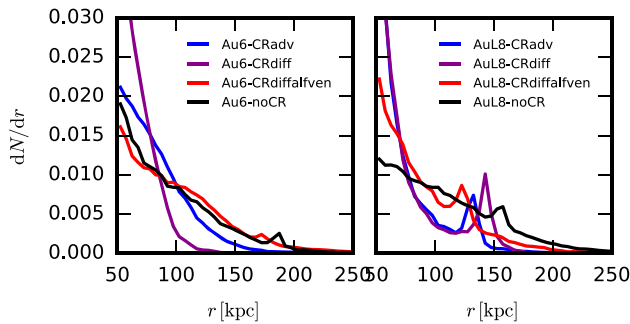

Figure 8. Radial distribution at a lookback time of 5 Gyr of the gas tracers which at present day are contained in stars. This figure traces the origin of the gas that evolves into stars at the present day. For AuL8 in the right-hand panel, the peaks around $R \sim 140$ kpc signal an ongoing merger.

quiescent, hydrostatic atmosphere in the halo in comparison to the former two models as can be seen from the larger ratios of $(P_{cr} + P_{th})/P_{kin, r}$ (yellow colours in Fig. 6). We verified that this result remains qualitatively similar over the entire redshift range $0 \le z \lesssim 1$ and we quantified the hydrodynamic effect of CRs on the gas flow with the distribution of radial inflow and outflow velocities in Fig. 7.

The simulations with CRs show narrower radial velocity distributions indicating reduced inflow and outflow velocities. This is the result of the process described above: the more elliptical and vertically expanded ISM in the CR runs precludes a geometrically preferred path of least resistance and slows down the outflows in all directions. Hence, there are no coherent outflows forming along the spin axis in the CR simulations. Because there are low-velocity outflows present in nearly all directions in these CR runs, this shocks the accreting gas and precludes the formation of most inflow channels that deliver gas from larger distances to the star-forming disc. The suppression of the inflow velocities is strongest for the CRdiff run because here CRs impact a larger region compared to the other runs. Interestingly, in the CRdiffalfven simulation we observe reduced infall velocities but similar or even larger outflow velocities in comparison to the fiducial AURIGA model due to the additional CR pressure-driven winds.

The immediate manifestation of this process is the suppression of the accretion of gas from larger distances in the CR runs as displayed in Fig. 8. In this figure, we show the distribution of radial distances at a lookback time of 5 Gyr of the gas which is at present day converted into stars of the stellar disc. In the fiducial AURIGA runs gas is

accreted from farther away in comparison to the CR counterpart simulations. This is the result of the modified gas accretion pattern on large scales mediated by the effects of the CRs on the structure of the gaseous disc on smaller scales. Note, this does not necessarily mean that SFRs in the CRdiff and CRadv run are suppressed as the outflow velocities are similarly reduced in these runs leaving enough gas to fuel star formation.

In summary, in the fiducial AURIGA and the CRdiffalfven simulations gas accretes relatively unimpeded from large distances whereas in the CRadv and CRdiff simulations the more spherically symmetric outflows and the CR pressurized gaseous haloes are able to held up the gas.

4 CIRCUMGALACTIC MEDIUM

We now turn to analyse the effects of CRs on the CGM properties in the different physics variants. In particular, we focus on how CRs shape the gas density distribution and impact the gas temperature profile of CGM gas by providing additional pressure support which manifests itself in high ratios of CR pressure to thermal pressure. To this extent we show in Fig. 9 from top to bottom maps of the gas surface density, the gas temperature, the ratio of CR pressure to thermal pressure, and the value of CR pressure for galaxy Au6. The orientation is chosen such that the gas disc is seen edge-on and the projection depth is the same as the horizontal/vertical extend (200 kpc). For a more quantitative comparison we accompany the maps by profiles of the same quantities for both galaxies in Fig. 10 as indicated by the panels' titles. For the CGM properties we have chosen logarithmically spaced spherical shells and averaged profiles over the last ten simulation outputs ($\sim$1 Gyr). Colour coding of the different physics variants is the same as in previous figures.

Looking at the first row of Fig. 9 and comparing the four different physics variants, we find that the CGM gas surface density in the CR runs outside the disc region ($R > 50$ kpc) is slightly higher in comparison to the fiducial AURIGA model. Most strikingly, the CGM gas density is significantly more spherical within 50 kpc in the CRdiff and CRadv runs compared to the fiducial AURIGA and the CRdiffalfven runs. Additionally, the CGM gas density is smoother in the CR runs in comparison to the noCR run. In the next subsections we address these morphological differences and highlight how CRs cause these changes of the CGM structure by investigating each model separately.
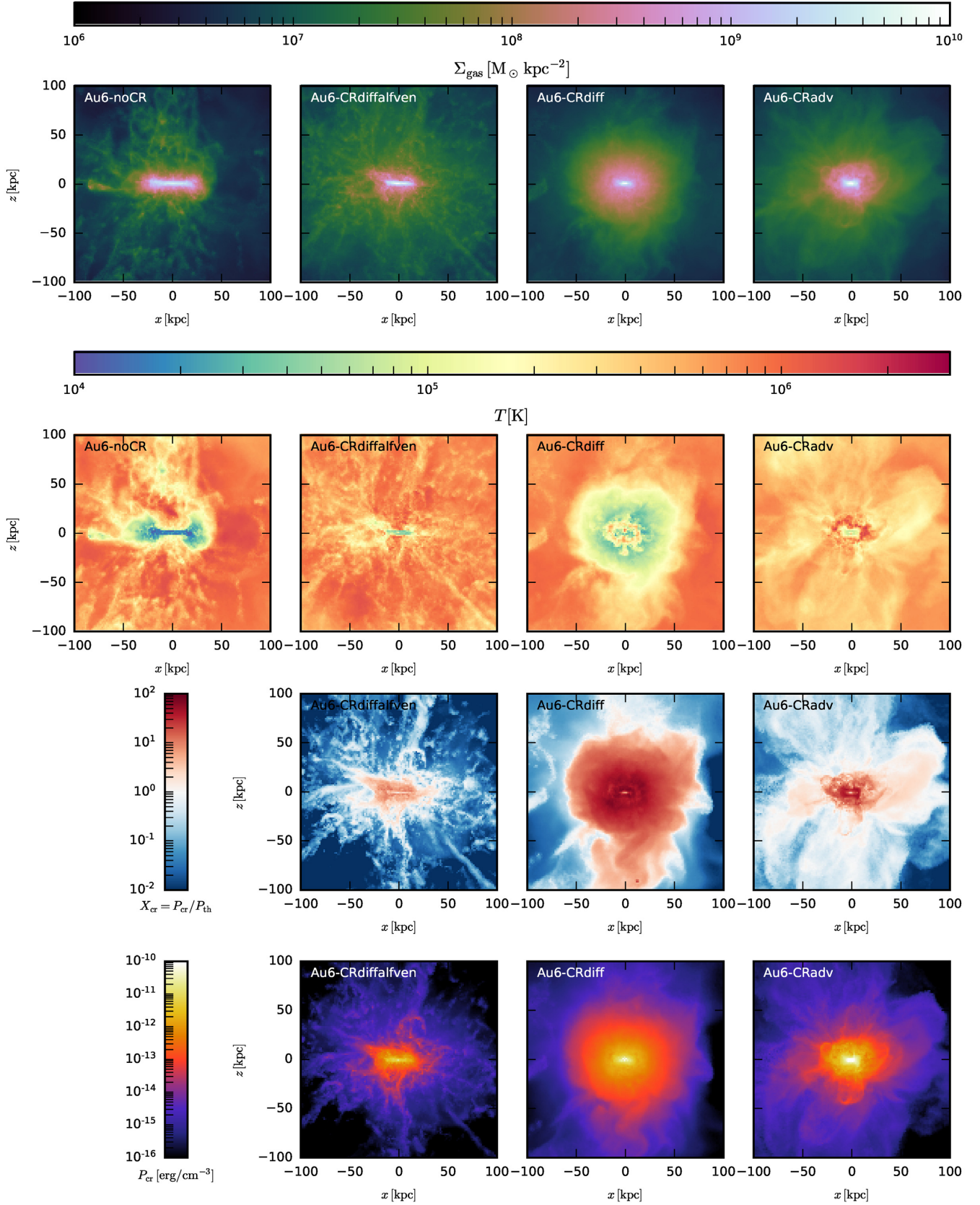
Figure 9. Maps of CGM properties for the four different physics runs of halo Au6 as indicated in each panel. From top to bottom we show the gas surface density, the gas temperature, the CR-to-thermal pressure ratio, and the CR pressure. The orientation of each panel is chosen to view the central disc edge-on and the projection depth of each panel is equal to its width, 200 kpc. Note the smooth gas distribution in the CR runs owing to the additional pressure of the CRs, which however differs considerably for our different variants of CR transport.
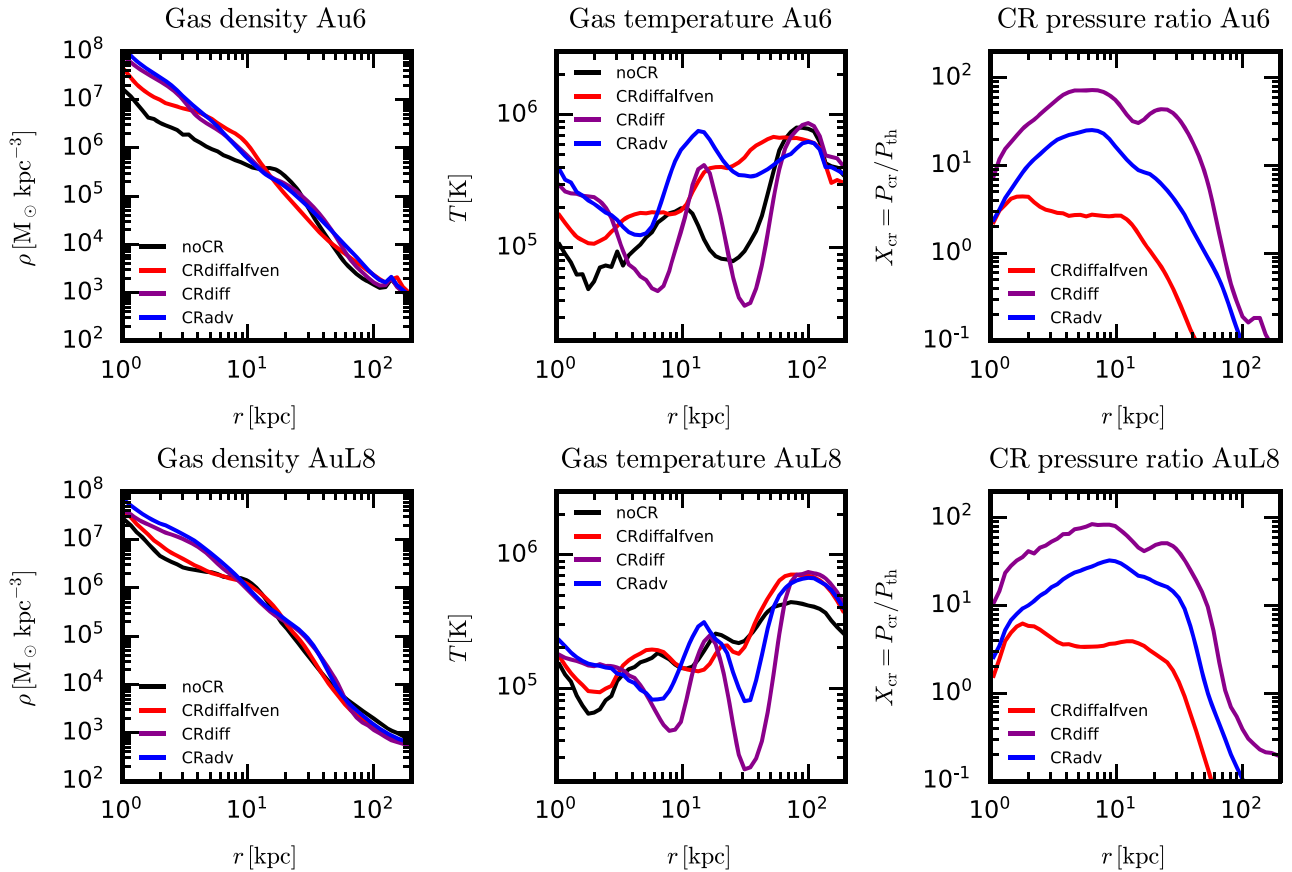
Figure 10. Comparison of the radial profiles of the gas density (left), gas temperature (middle panel), and magnetic field strength (right) in the four different physics variants of Au6 (upper panel) and AuL8 (lower panels). The profiles represent time averages over the last 10 simulation outputs ($z \sim 0.1$, $t \sim 1$ Gyr).

4.1 AURIGA – no cosmic rays

The baseline model for our comparison is the fiducial AURIGA model which has a highly structured CGM with cool, high-density patches coexisting next to hot low-density regions (left-hand panels in Fig. 9, see also van de Voort et al. 2019). The clumpy CGM morphology is further reflected in a broad gas density distribution with tails to large gas densities as shown in Fig. 11. Here, we show the density distribution of all four runs in two different concentric shells of width 50 kpc as indicated by the panel titles. The left two panels show galaxy Au6, the right two AuL8.

4.2 Cosmic ray advection

The most simple approximation for CR transport physics is the advection of CRs, which neglects all active CR transport processes. Therefore, all CRs in the CGM have been transported there by outflows. In the CRadv run the CGM is significantly more spherical within 50 kpc, smoother and of slightly lower temperature (right-hand panel of Fig. 9) when compared to the fiducial AURIGA run owing to the additional CR pressure. Especially far away from the disc at $R \sim 50$ kpc the density is slightly enhanced in comparison to the fiducial run. The inclusion of CRs leads to cooler gas temperatures even at distances of $R \sim 100$ kpc where CR pressure is approximately in equilibrium with the thermal pressure. The additional CR pressure smoothes out almost all small-scale high density peaks in the CGM gas which quantitatively leads to a narrower gas density distribution in Fig. 11.

4.3 Cosmic ray diffusion

Allowing for CR anisotropic diffusion alters the properties of the CGM dramatically but with similarities to the CRadv run. We find that the CGM gas density is even more spherical within 50 kpc compared to the CRadv run, highly CR pressure dominated and of much cooler temperatures. In this run, CRs are allowed to diffuse and thus are able to affect the CGM at larger distances from the disc, thus the CR pressure dominated halo is larger in size compared to the CRadv run. Furthermore, the CR pressure contribution is higher compared to the CRadv run (see also discussion in Sections 3.2 and 6.3) leading to an even smoother CGM (see narrow gas distribution in Fig. 11 for this run). The additional CR pressure that in this run dominates the CGM out to radii of $R \sim (50–100)$ kpc supports the gas against gravitational collapse in the absence of thermal pressure support and thus explains the low CGM temperatures which coincide with the regions where CR pressure dominates. Fig. 10 shows that in a region of $R < 50$ kpc the CR pressure is a factor of ~ 10 larger than the thermal pressure.

4.4 Cosmic ray diffusion with Alfvén wave cooling

The CRdiffalfven model in turn reveals a CGM morphology similar to the fiducial AURIGA model (although with noticeable differences) and shows clear differences in comparison to the CRdiff and CRadv run. In comparison to the AURIGArun (CR runs), the CGM features smoother (more structured) density peaks and the central
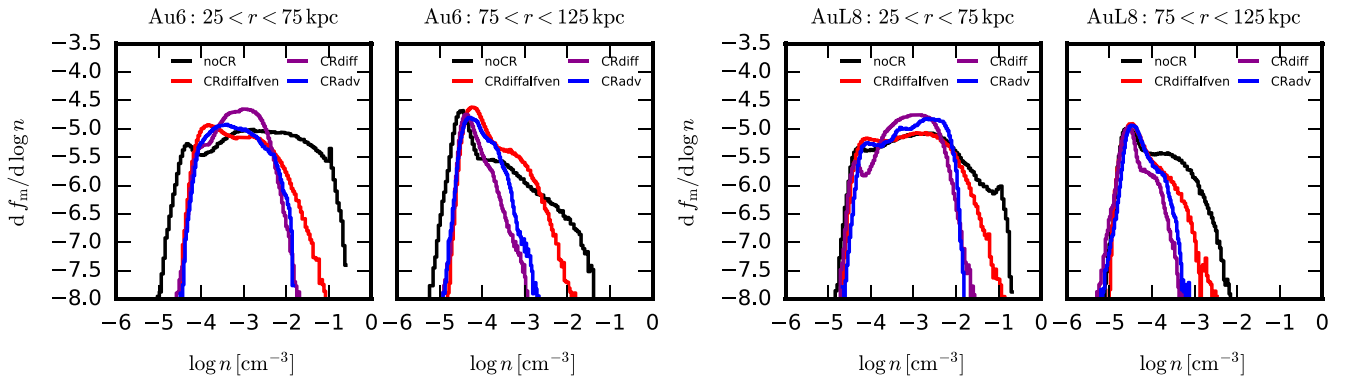
Figure 11. Distribution of gas density in two different 50 kpc wide spherical shells for the Au6 halo in the two left most panels and the Au8 halo in the two right most ones. The CRadv and CRdiff runs exhibit narrower density distributions in comparison to the other two models indicating a smoother CGM.

CGM appears discy. Again, the additional CR pressure explains the smoother gas density compared to the AURIGA model while the Alfvén cooling explains the weaker damping compared to the CRdiff and CRadv runs. Therefore in Fig. 11, the gas density distribution of the CRdiffalfven run lies between the AURIGA model and the other two CR models.

In comparison to the CRdiff run the CGM is much hotter and shows even less cold regions compared to the fiducial run. In fact, the profiles (middle panels in Fig. 10) show that Au6 has a hotter CGM in the CRdiffalfven run compared to the AURIGA run. AuL8 on the other hand shows a similar CGM temperature. The slightly enhanced CGM temperature in Au6 is presumably due to the additional Alfvén heating of the CRs and the fact that Au6 had a recent burst of SF injecting CRs into the CGM. This burst is not present in AuL8. From the lower panels in Fig. 9, we can further see that the CR pressure dominates the central regions (except for the disc) while for most of the CGM gas the CR pressure is in equilibrium with the thermal pressure (see also right-hand panels in Fig. 10). This is different to the other CR runs and a manifestation of the Alfvén wave cooling in which the CRs lose an e-folding of their initial energy as they diffuse a scale height into the CGM.

4.5 CGM pressure support

In Fig. 12, we compare in detail the different pressure components (upper panels) and their contribution to the total pressure (lower panels) in the CGM. We compare magnetic pressure (orange), 'kinetic pressure' (red), thermal pressure (blue), and CR pressure (green) to the total pressure (black) in spherical shells as we have explained for Fig. 10. From left to right we show the fiducial AURIGA noCR, the CRdiffalfven, the CRdiff, and the CRadv runs.

In the region influenced by accretion on to the disc as well as the disc itself (within a few tens of kpc) the gas is rotationally supported (i.e. has a dominating kinetic pressure) in all runs while the other pressure components, i.e. thermal, magnetic, and CR pressure, are roughly in equipartition contributing each about ∼10 per cent to the total pressure. In the outskirts at radii larger than $R > 20$ kpc we find that all the runs become increasingly thermal pressure dominated except for the CRdiff run where CR pressure dominates and the thermal pressure becomes negligible. Only close to the virial radius the thermal pressure becomes important again which was already noted by the huge CR pressure dominated halo in Fig. 9. This confirms our previous findings that the cool region in the CGM at these radii is entirely CR pressure dominated.

4.6 Temperature–density relation

Our findings for the structure and morphology of the CGM are summarized in Fig. 13 showing the temperature–density distribution of the CGM gas in the radial range $50 < R < 200$ kpc. While at first glance differences between the fiducial run and the CR runs are small, one notices that the hot phase in the CR runs tends to inhabit regions of lower temperature. In more detail, we find that the CRdiffalfven runs show a larger spread in temperature at any density compared to the noCR run which shows the importance of CR Alfvén heating. This figure further shows that for the CRdiff run gas at $\rho \sim (10^{-4}–10^{-3})$ cm^{-3} piles up at a temperature of $T \sim 10^{4.5}$ K. We interpret this as the CR pressure keeping this gas from falling on to the main galaxy. Finally, we find that in the CRadv run the CR pressure causes a different slope of the ρ–T relation for the non-star-forming gas at $T \sim 10^4$ K due to the CR pressure support at the disc–halo interface.

Thus, CRs do not only affect the properties of the gas disc as we have seen in Fig. 3 but also the gas morphology of the CGM even at large distances close to the virial radius of the halo. The analysis in this section reinforces the need to better understand the physics of CR transport, as we have shown here that different variants of approximating it have a strong impact on the stellar structure and especially the properties of the CGM.

5 FAR-INFRARED–GAMMA-RAY RELATION

Finally, after establishing the differences and similarities between the three variants of CR transport in our simulations we connect our results to the most directly observable CR proton properties of galaxies, namely hadronic gamma-ray emission that arises from inelastic collisions of CRs with the ambient ISM. To this end, we compare in Fig. 14 the gamma-ray luminosities in the Fermi band (0.1–100 GeV) to the SFR for all the main disc galaxies (big black bordered symbols) in comparison to observational data as indicated in the caption. Additionally, we also show gamma-ray luminosities for the dwarf galaxies within the zoom region (small coloured dots). Note that these dwarfs are not satellite galaxies as they are not part of the main halo but proxies of field dwarfs in the Local Volume. Note that our homogeneous observational sample in the Fermi band spans an energy range of 0.1–100 GeV leading to somewhat higher gamma-ray luminosities in comparison to previous observational data collections (cf. Lacki et al. 2011, who use the smaller energy band between 1 and 100 GeV).
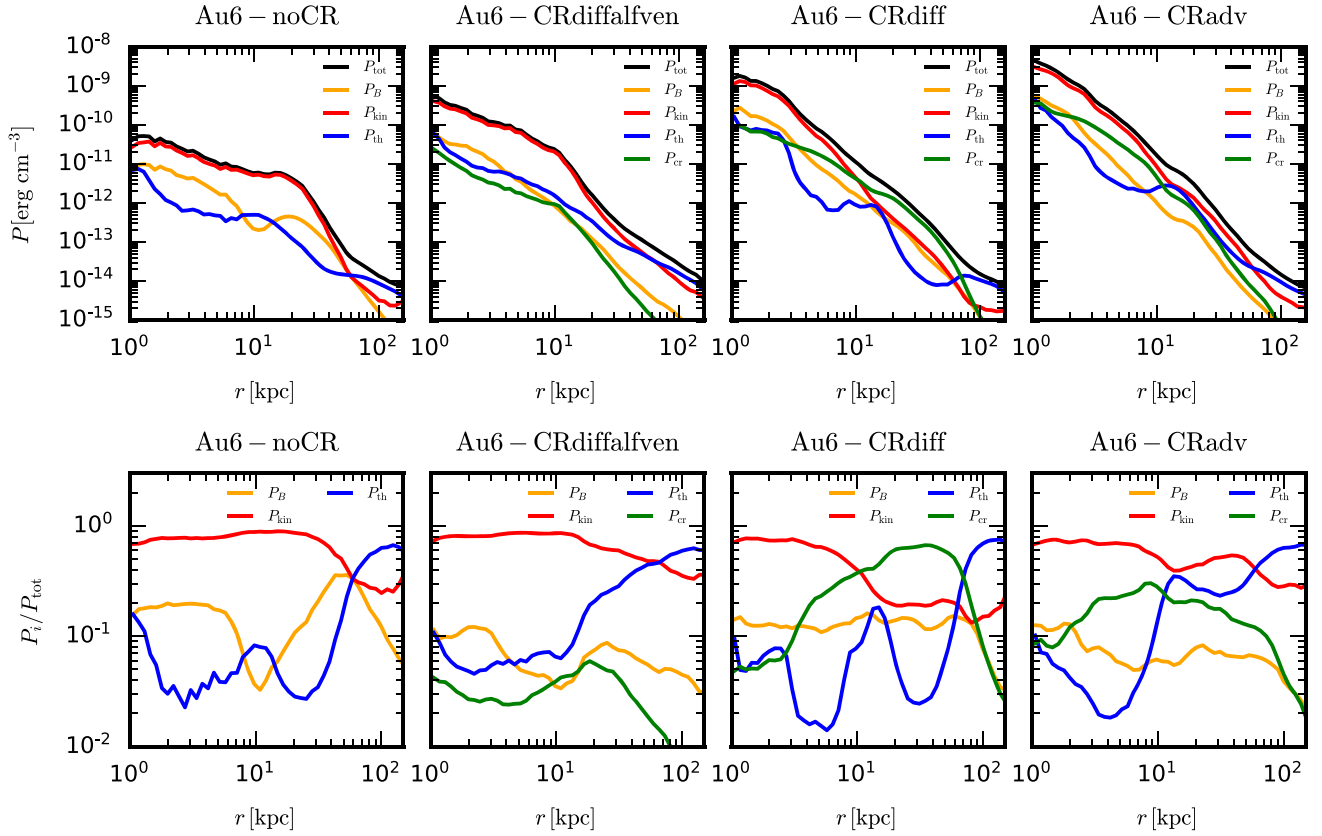
Figure 12. Radial profiles of different pressure components for the four different physics variants of halo Au6. The upper panels compare absolute pressure profiles of the magnetic ($P_B = \boldsymbol{B}^2/(8\pi)$, orange line), 'kinetic' ($P_{kin} = \rho \boldsymbol{v}^2/2$, red), thermal ($P_{th} = (\gamma - 1)\varepsilon_{th}$, blue), and CR ($P_{cr} = (\gamma_{cr} - 1)\varepsilon_{cr}$, green) components as well as the total pressure (black). Lower panels compare the relative pressure contributions to the total pressure.
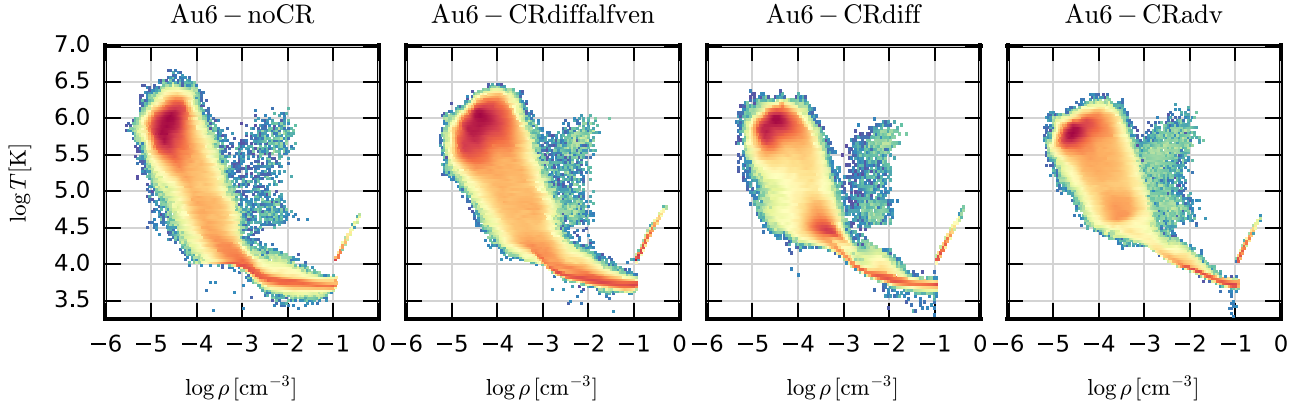

Figure 13. Present-day temperature–density phase diagrams of CGM gas ($50 < R < 200$ kpc) for the four different physics runs of galaxy Au6. Colour coding shows the logarithm of the mass weighted probability density where red colours indicate high and blue colours low probability.

The total far-infrared (FIR) luminosity (8–1000 μm) is a well-established tracer of the SFR of spiral galaxies (Kennicutt 1998) with a conversion rate

$$\frac{\mathrm{SFR}}{\mathrm{M_\odot\,yr^{-1}}} = \epsilon\, 1.7 \times 10^{-10}\, \frac{L_{8-1000\,\mu\mathrm{m}}}{\mathrm{L_\odot}}. \qquad (4)$$

This SFR–FIR conversion assumes that thermal dust emission is a calorimetric measure of the radiation of young stars, and the factor

$\epsilon = 0.79$ derives from the Chabrier (2003) IMF (Crain et al. 2010). While this conversion is reliable at $L_{8-1000\,\mu\mathrm{m}} > 10^9\,\mathrm{L_\odot}$, it becomes progressively worse at smaller FIR luminosities due to the lower metallicity and dust content, which implies a low optical depth to IR photons and invalidates the calorimetric assumption (Bell 2003). We have verified that down to SFRs comparable to those of M31 ($\sim$0.3–0.4 $\mathrm{M_\odot\,yr^{-1}}$) our conversion still holds. The SFR of M31 derived here is in good agreement with SFRs derived using a combination of Hα
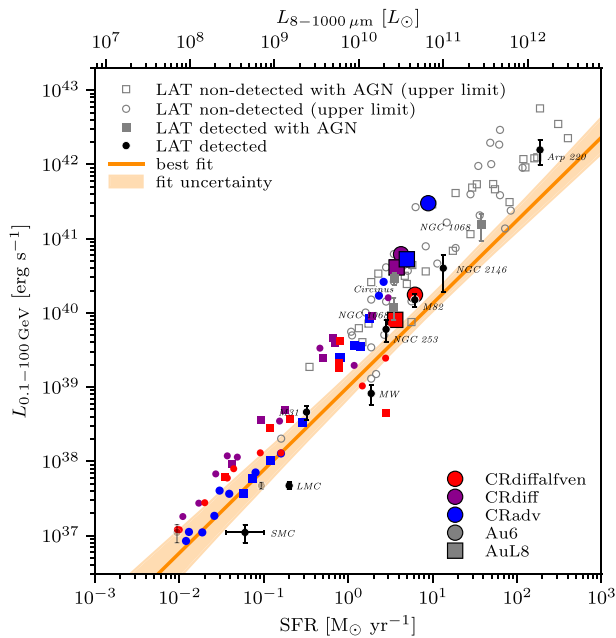
Figure 14. Correlation of the gamma-ray luminosity ($L_{0.1-100\ \mathrm{GeV}}$) with the SFR and with the FIR luminosity ($L_{8-1000\ \mathrm{mm}}$) of star-forming galaxies. We compare our six simulated CR models (differently coloured symbols delineate Au6 and AuL8 haloes) and plot central galaxies (thick symbols) and dwarf galaxies (thin symbols). Upper limits on the observable gamma-ray emission by Fermi-LAT (open grey symbols; Rojas-Bravo & Araya 2016) are contrasted with gamma-ray detections from star-forming galaxies only (solid black) and with AGN emission (filled grey); data are taken from Ackermann et al. (2012), except for NGC 2146 (Tang, Wang & Tam 2014) and Arp 220 (Griffin, Dai & Thompson 2016; Peng et al. 2016). For the two lowest SFR galaxies, the SMC and LMC we use grey data points for the observed FIR luminosities (top axis) and solid black data points for the SFRs derived using H α and UVBI photometry. Note that only the CRdiffalfven runs fall on the best-fitting observational FIR-gamma-ray correlation (orange).

and 24 μm emission, a combination of far-ultraviolet, 24 μm, and the total infrared emission which yield $\sim(0.35-0.4)\pm0.04\ \mathrm{M_\odot\ yr^{-1}}$ (see Rahmani, Lianou & Barmby 2016).

We show the observed FIR luminosity of the LMC and SMC with grey data points in Fig. 14, while SFR estimates for the LMC and SMC are shown with solid black data points. Those are derived by combining H α and FIR emission (assuming a Chabrier IMF, Wilke et al. 2004) or UVBI photometry (Harris & Zaritsky 2009) and range for the SMC between 0.036 and 0.1 $\mathrm{M_\odot\ yr^{-1}}$, while the LMC forms 0.2 $\mathrm{M_\odot\ yr^{-1}}$ of stars (Harris & Zaritsky 2009). We refer the reader to Pfrommer et al. (2017b) for more details on the FIR-to-SFR conversion and to Pfrommer & Enßlin (2004) for the computation of the gamma-ray emission resulting from hadronic proton interactions with the ambient ISM.

We find that at the MW mass scale or vice versa at a FIR luminosity of $\sim 5\times10^{10}$ $\mathrm{L_\odot}$ the three CR models predict very different gamma-ray luminosities. Whereas the CRdiffalfven runs are in good agreement with the observational data, especially for NGC 253 and M82, the other two models lie above the best-fitting observational relation of Rojas-Bravo & Araya (2016) and are barely consistent with upper limits from Fermi–LAT (grey open symbols). This is interesting as the same physical models for CR transport (CRadv and CRdiff) yield hadronic gamma-ray luminosities in agreement with the best-fitting observational relation for the collapsing halo

initial conditions (Pfrommer et al. 2017b). Unlike our cosmological simulations, these idealized setups produce more extended gas and stellar discs. As a result the inner gravitational potential due to the kinematically cold distribution of central stars is shallower in these idealized models in comparison to our cosmological simulations in the CRdiff and CRadv models. Such a massive central stellar distribution in our cosmological simulations injects too many CRs and compresses the gas to a level that the CRs overproduce the hadronic gamma-ray emission. Clearly, different types of feedback (radiation, supernovae) are necessary to act in tandem with CRs to prevent the formation of these dense cores at high redshift in our cosmological simulations.

At lower SFRs and accordingly lower FIR luminosities, the differences between the three models become smaller and both the CRdiffalfven and the CRadv model agree with the observed relation of Rojas-Bravo & Araya (2016) while the CRdiff model produces a somewhat elevated level of gamma-ray luminosity. We attribute this behaviour to the lower injection rate of CRs at these SFRs and higher escape fractions of CRs from these low-mass galaxies (Zhang, Peng & Wang 2019). Our CRdiffalfven model is able to explain the distribution of luminosities of the MW and M31. In particular at SFRs comparable to M82 and NGC 253 only this model matches observed gamma-ray luminosities.

However, the simulations of all CR models in Fig. 14, including the CRdiffalfven model, do not agree with the observed SFRs and gamma-ray luminosities of the LMC and SMC. This can either be interpreted as an overprediction of the simulated gamma-ray luminosity (by a factor of about 2–2.6 for the LMC and about 6–8 for the SMC depending on the specific simulated counterpart), an underprediction of the simulated SFR (by a factor of 2–10 for the LMC and 2–6 for SMC), or a combination of both. There are several reasons that could be responsible for this. Among those is the emission of CR streaming, which will be studied in a forthcoming paper. In fact, CR streaming in combination with diffusion might lead to an increased effective CR transport speed which might decrease the gamma-ray luminosity in dwarf galaxies (e.g. Salem, Bryan & Corlies 2016; Jacob et al. 2018; Chan et al. 2019). Moreover, we would like to emphasize that the LMC and SMC are satellite galaxies of the MW, which are most likely at their first infall and in an interacting state (Harris & Zaritsky 2009). This might lead to higher SFRs in comparison to the isolated, non-satellite dwarf galaxies studies in Fig. 14. While the CR production scales with the SFR and accordingly the gamma-ray luminosity, it is a matter of time-scales involved whether the gamma-ray luminosity closely follows the measured SFR (which is intrinsically uncertain by a factor of two for the LMC, see e.g. Harris & Zaritsky 2009). In fact the LMC SFR shows a strong burst in the last few 10^7 yr (cf. fig. 11 of Harris & Zaritsky 2009). For such a recent burst we do not expect that the gamma-ray production had time to fully react as the lifetime of galactic CRs is of the order of $\gtrsim 3\times10^7$ yr (e.g. Simpson & Garcia-Munoz 1988; Lipari 2014).

Finally, our simulated points agree with the mean power-law relation. It is unclear whether the true observational relation continues along the power-law relation with the LMC and SMC representing outliers or whether the lower gamma-ray luminosities of the LMC and SMC indeed signal a cut-off or change in slope of this relation.

We note that at low SFRs the CRadv model produces the lowest gamma-ray luminosities while at high SFRs this model shows the opposite effect. This outcome can be explained by a different behaviour of the adiabatic processes in haloes of different masses. Fig. 4 of Pfrommer et al. (2017a) shows that adiabatic losses dominate in smaller haloes corresponding to lower SFRs while

adiabatic gains prevail in larger haloes. Especially, at low SFRs the adiabatic losses in the CRadv model are larger compared to those in the CRdiff model which explains the low gamma-ray luminosities of this model at low SFRs.

Note that our CR models reproduce the observed relation for Galactic values of the diffusion coefficient ($\kappa_\parallel = 10^{28}$ cm² s⁻¹) or even without CR diffusion (for our CRadv model). This is in stark contrast to the FIRE-2 simulations that require diffusion coefficients of $\kappa_\parallel > 3 \times 10^{29}$ cm² s⁻¹ to be consistent with the gamma-ray observations (Chan et al. 2019; Hopkins et al. 2020). These differences can be traced back to the ISM model of AURIGA, which supports a CR transport with a single diffusion coefficient while the highly structured multiphase ISM of FIRE-2 would require to fully model CR streaming with various wave damping mechanisms that dominate in the cold (ion-neutral damping) and warm/hot phases (non-linear Landau damping), respectively.

In conclusion, observable scaling relations such as the gamma-ray–FIR relation offer promising tools for distinguishing physically valid models and might help to constrain the values of free sub-grid model parameters (e.g. Buck, Dutton & Macciò 2019). However, a detailed model comparison to observations like, e.g. the CGM properties derived from the COS-HALOS survey (Tumlinson et al. 2013) needs to include careful post-processing of the simulations which is outside the scope of this study and thus left for future research.

6 DISCUSSION

6.1 Comparison to observations

For galactic CRs there exist three different observables which can be used for scrutinizing our model predictions: the local energy density of CRs, the gamma-ray luminosity, and the CR grammage, $X_s = \int_{\text{source}}^{\text{observer}} \rho_{\text{nuclei}} \mathrm{d}l_{\text{CR}}$. In this paper, we have calculated the former two observables because those can be robustly derived from our models whereas the latter quantity is a gyro-radii averaged integration of the target density along the path of individual CRs and strongly depends on a number of properties. Among those are the exact initial CR energies that are mapped on to the observed CR spectra, the CR source distribution, the variability of CR injection (both in time and space), the exact topology of the magnetic field (at large and small scales, which are necessarily unresolved in current cosmological simulations and would have to be modelled sub-grid) as well as the exact small-scale density distribution in the ISM along the CR path. Therefore, deriving a meaningful value for the CR grammage in our simulations is beyond the scope of this paper and we leave such a detailed comparison for future studies.

Comparing our model observables for the local energy density of CRs (right panels of Fig. 4) we find that the CRdiffalfven model results in the lowest CR energy densities. At the solar circle ($r_{xy} \sim$ 8 kpc), we find a value of $\epsilon_{\text{cr}} \sim 2$ eV cm⁻³ for AuL8 and $\epsilon_{\text{cr}} \sim 4$–5 eV cm⁻³ for Au6. A fair comparison to MW measurements needs to account for the fact that both model galaxies show slightly higher SFRs of $\sim$2 for AuL8 and $\sim$3 for Au6 (see e.g. Fig. 14) in comparison to MW rates of $\sim$1.65–1.9 M$_\odot$yr⁻¹ (e.g. Chomiuk & Povich 2011; Licquia & Newman 2015). Because the SFR is directly proportional to the CR energy input in our models, we expect approximately 1.3 to two times lower CR energy densities in those models at SFRs comparable to the MW. This leaves us with CR energy densities of $\sim$1.6 eV cm⁻³ for AuL8 and $\sim$2–2.7 eV cm⁻³ for Au6. Given that inferred observational results are uncertain by a factor of $\sim$2 (see e.g.

discussion in Cummings et al. 2016) we conclude that the rescaled CR energy densities of those models are in reasonable agreement with estimates for the MW of about $\epsilon_{\text{cr}} \lesssim 1.8$ eV cm⁻³ at the solar circle (e.g. Boulares & Cox 1990; Webber 1998; Cummings et al. 2016). By contrast, the CRdiff and CRadv models show much higher CR energy densities.

We have extensively compared and discussed the gamma-ray luminosities of our model galaxies in comparison to observations in Fig. 14. Above an SFR of $\sim$0.35 M$_\odot$yr⁻¹ (comparable to that of M31) our CRdiffalfven model is in excellent agreement with the Fermi observations in the energy band 0.1–100 GeV. By contrast, the other two models show much higher gamma-ray luminosities and overpredict the observed values. Below an SFR of 0.35 M$_\odot$yr⁻¹ there are only two data points for the SMC and LMC, which have lower gamma-ray luminosities than our models. As discussed above, the SMC and LMC are satellites of the MW which might either have enhanced SFRs in comparison to non-satellite dwarf galaxies (Harris & Zaritsky 2009) effectively shifting them to the right in Fig. 14 or show lower gamma-ray luminosities in comparison to the observational relation of Rojas-Bravo & Araya (2016) due to an increased gamma-ray variance at low SFRs. Therefore, the paucity of gamma-ray data at low SFRs precludes strong conclusions about the correctness of models and shows the importance of obtaining better observational gamma-ray constraints at low SFRs.

We conclude that the CR energy density at the solar circle and the gamma-ray luminosities in our CRdiffalfven model reproduce the observational data well while our CRdiff and CRadv models overpredict both observational constraints.

6.2 CR diffusion coefficient

The pressure-carrying CR distribution at GeV energies propagates via streaming with Alfvén waves and diffusion relative to the frame of those waves (Kulsrud & Pearce 1969; Amato & Blasi 2018; Thomas, Pfrommer & Enßlin 2020). If this microscopic CR transport were modelled in the form of CR diffusion, this would imply a spatially and temporarily varying CR diffusion coefficient because of the varying Alfvén speed and the various wave damping mechanisms that dominate in different phases of the ISM and modulate the coupling strength of CRs to the ambient plasma (Jiang & Oh 2018; Thomas & Pfrommer 2019): weak wave damping implies a strong coupling and causes the CRs to stream with Alfvén waves whereas strong wave damping leaves less waves to scatter CRs so that CR diffusion prevails. If this complex CR transport were modelled with a constant, isotropic CR diffusion coefficient, it assumes typical values for GeV CRs of $\kappa_{\text{iso}} \sim (1 - 3) \times 10^{28}$ cm² s⁻¹ as we will argue below.

The relation between κ_{iso} and the CR diffusion coefficient along the magnetic field, $\kappa_\parallel$, depends on the exact magnetic field configuration. For a turbulent field, $\kappa_{\text{iso}} = \kappa_\parallel/3$, whereas if CR transport along the homogeneous magnetic field dominates, we have $\kappa_{\text{iso}} = \kappa_\parallel$. For CR feedback to be active, CRs move along open field lines from the disc into the halo (that are either vertically aligned through an outflow or via the Parker instability) so that $\kappa_{\text{iso}} \sim \kappa_\parallel$ in the regime of interest where galactic winds are accelerated by the CR pressure gradient. There is evidence that CRs escaping from the disc into the halo excite the streaming instability (Kulsrud & Pearce 1969; Evoli et al. 2018), which limits the drift speed to that of the Alfvén frame, which is $\sim$30 km s⁻¹ at the disc–halo interface and increases to $\sim$300 km s⁻¹ at the virial radius. This coincides with the diffusion velocity $v_{\text{diff}} \sim 30$ km s⁻¹ $\kappa_{28} L_{3\,\text{kpc}}$, where $\kappa_{28} = 10^{28}$ cm² s⁻¹ is the CR diffusion coefficient and $L_{3\,\text{kpc}}$ is the CR gradient length, justifying our choice of the CR diffusion coefficient.

A diffusion coefficient for CRs in the Galactic disc can also be estimated from CR propagation models and observations of synchrotron radiation and/or the ratio of secondary to primary nuclei (Strong & Moskalenko 1998; Ptuskin et al. 2006; Ackermann et al. 2012; Tabatabaei et al. 2013; Amato & Blasi 2018). In the Galactic halo, CRs have a scale height of ∼3 kpc and their residency time in the thick disc is inferred to be $\tau \sim 3 \times 10^7$ yr as obtained from measurements of the ratio of secondary-to-primary CR nuclei (Lipari 2014; Evoli et al. 2020). Thus, the diffusion coefficient of GeV CRs is given by $\kappa_{iso} \sim H^2/(3\tau) \sim 3 \times 10^{28}$ cm^2 s^{-1}. This order of magnitude estimate for κ_{iso} is confirmed by several different studies of CR propagation, including GALPROP simulations that aim to reproduce the Fermi gamma-ray sky (Porter, Jóhannesson & Moskalenko 2017; Jóhannesson, Porter & Moskalenko 2019). The recently discovered hardening of the momentum power-law slope of the CR proton spectrum at low Galactocentric radii could be a signature of anisotropic diffusion in the complex Galactic magnetic field with $\kappa_{\parallel} = 1 \times 10^{28}$ cm^2 s^{-1}, as suggested by DRAGON2 simulations (Cerri et al. 2017; Evoli et al. 2017). Finally, the flux of unstable secondary CR nuclei in the recent AMS-02 data, produced by spallation processes in the ISM, can be used to constrain the residence time of CR inside the Galaxy, yielding identical values for the diffusion coefficient (Evoli, Aloisio & Blasi 2019; Evoli et al. 2020).

The exact numerical value of $\kappa_{\parallel}$ determines the CR diffusion time-scale in the disc and thus controls the amount of dynamical impact of CRs on the galaxy. A large value of $\kappa_{\parallel}$ leads to short diffusion time-scales and a quick escape of CRs from the disc. We have tested the impact of a three times higher value of the CR diffusion coefficient ($\kappa_{\parallel} = 3 \times 10^{28}$ cm^2 s^{-1}) on the results obtained here. Fig. 15 shows from top to bottom face-on and edge-on projections of the stellar disc's light, the gas surface density and edge-on projections of the CGM CR-to-thermal pressure ratio, X_{cr} for the fiducial models (with $\kappa_{\parallel} = 1 \times 10^{28}$ cm^2 s^{-1}) and those with a three times higher diffusion coefficient. We confirm the expectation that a higher value of $\kappa_{\parallel}$ leads to a smaller dynamical effect of CRs on galaxy properties such as the reduction in stellar disc size in the CRdiffalfven model (upper panel in Fig. 15). Here, the faster CR transport also causes faster Alfvén cooling which diminishes the dynamical impact of CRs so that the gas distribution looks similar to the noCR model (cf. Figs 1 and 3). This effect is less pronounced in the CRdiff model as here the combination of CR energy conservation (during the diffusion step) and their higher escape speed lead to a larger CR pressure-dominated halo (bottom right panels of Fig. 15). This CR pressure dominated halo in turn prevents the gas from efficiently cooling on to the disc. These simulations reinforce our main results that small variants of CR transport can have substantial impact on the resulting galaxies.

6.3 Implications for CR transport in galaxies and the CGM

Our analyses of CR feedback have several important implications for CR transport and the excitation of CR driven instabilities. The CR pressure in the CRdiff model dominates over the thermal pressure up to large radii ($r \lesssim 80$ kpc). In such a quasi-hydrostatic atmosphere, the CGM necessarily attains a comparably smooth distribution. By contrast, the CR pressure distribution in the CRadv model reflects the dominating modes of transport and cooling processes. Advection of CRs with the galactic outflows along streamlines implies a highly structured CR distribution (Fig. 9). Turbulent mixing in the CGM (Pakmor et al. 2019) causes a smoother CR distribution, in particular at large radii $r \gtrsim 50$ kpc.

Additionally including CR diffusion smooths the CR distribution considerably as a result of two effects: (i) CR diffusion on cosmological time-scales results in a root mean square displacement of 25 kpc $\sqrt{\kappa_{28} t_{10\,Gyr}}$ along the magnetic field lines and (ii) perpendicular transport is achieved through field line wandering. Assuming that the velocity differences between neighbouring points follow a Gaussian distribution, we obtain explosive Richardson diffusion with a displacement $\langle x^2 \rangle \propto t^3$ up to the injection scale of turbulence (and standard diffusion above this scale), which smooths the CR distribution in the CGM considerably (Fig. 9).

Most surprisingly, by additionally accounting for CR Alfvén wave losses, the CR pressure distribution becomes highly structured. As CRs diffuse a scale height, they loose an e-folding of their initial energy. This distance can be substantially increased if CRs are predominantly advected with the gas. As their diffusive transport reaches the effective scale height, they cool quickly and subsequent turbulent mixing is greatly suppressed. Hence, they should trace out individual streamlines of the gas in their pressure as well as in the CR-to-thermal pressure ratio (see Fig. 9).

We have seen in Fig. 12 that the CR and magnetic pressures vary by four orders of magnitude but trace each other within a factor of 5 out to the virial radius. This remarkable finding has severe consequences for the existence of current driven CR instabilities. The condition for exciting the hybrid, non-resonant CR instability is $\epsilon_{cr}/\epsilon_B \gtrsim 2c/v_d$ (Bell 2004), where v_d is the drift speed of CRs that is close to the Alfvén speed as explained above. Because our CR and magnetic energy densities closely trace each other, the Bell instability is not excited and hence, no additional growth of the magnetic field is expected from this plasma effect. This also implies that the adopted diffusion coefficient remains valid and is not lowered to the classical Bohm limit due to strong Bell fluctuations, which would scatter CRs off magnetic irregularities at every gyro orbit. This fast CR scattering would manifest itself as a much reduced CR diffusion coefficient by about seven orders of magnitudes, which would effectively imply a transition to the CRadv model.

6.4 Comparison to previous work

6.4.1 Effects on the central galaxy

In this study, we found that CRs have little effect on global galaxy properties such as stellar mass and SFR. All our galaxies exhibit a rotationally supported gas disc dominated by the kinetic pressure (Fig. 12) and a mostly thermally supported CGM in the halo ($R \gtrsim$ 75 kpc). The CRdiff run additionally shows a transition region at the disc–CGM interface ($20 < R < 75$ kpc) where CRs dominate the pressure budget, permitting a lower CGM temperature (see also Butsky & Quinn 2018, Fig. 6). On the other hand, in the CRadv run this transition region shows an equilibrium of CR pressure with the thermal and the kinetic pressure. This agrees qualitatively with results obtained by Salem et al. (2016, Fig. 2) and the recent findings of Hopkins et al. (2020) despite the large differences in the diffusion coefficients used (this work: $\kappa_{\parallel} = 1 \times 10^{28}$ cm^2 s^{-1} versus 'best fit' $\kappa_{\parallel} = 3 \times 10^{29}$ cm^2 s^{-1} in FIRE-2).

While qualitative agreement between our results and the ones presented by the FIRE group exist, the fundamental differences in the value of the diffusion coefficient is a result of the physical consequences of a different treatment of the ISM in the simulations. As detailed in Section 6.2, our choice for $\kappa_{\parallel}$ is justified by CR propagation studies (Cerri et al. 2017; Evoli et al. 2017; Porter et al. 2017; Evoli et al. 2019, 2020; Jóhannesson et al. 2019) and is in line with other simulation analyses of galaxies forming in a cosmological
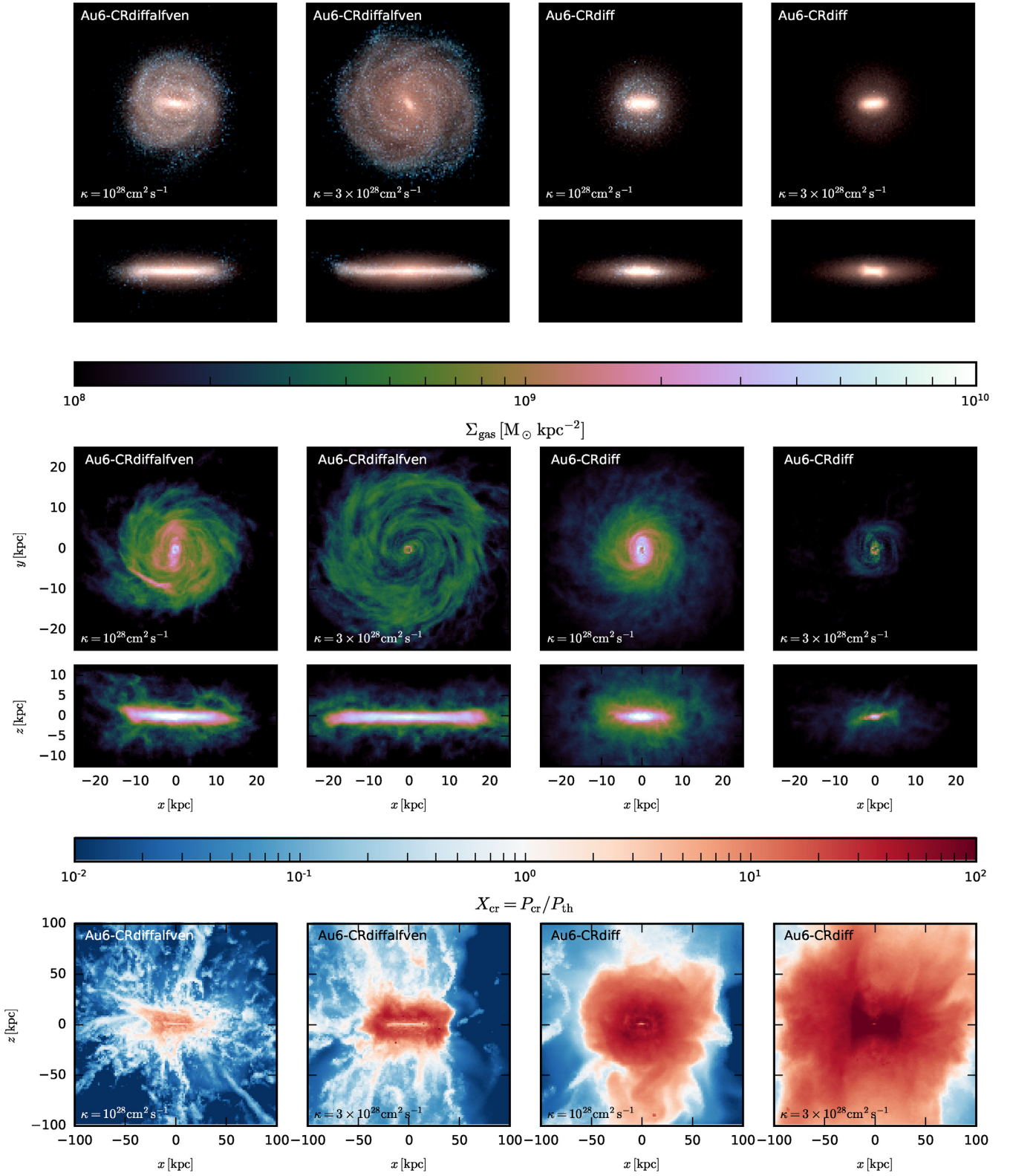
Figure 15. Face-on and edge-on projection of the stellar light at $z = 0$ (upper panels), the gas surface density (middle panels), and the CR-to-thermal pressure ratio, X_{ncr} (bottom panels), for the CRdiffalfven and the CRdiff model for two different diffusion coefficients as indicated in the panels. See caption of Figs 1 and 3 for further details.

environment (Salem et al. 2016). By contrast, the favoured diffusion coefficients in the FIRE-2 simulations are a factor 10–30 larger than those studied here and inferred in the CR literature. In fact, we believe that the choice of such a large diffusion coefficient in the FIRE-2 simulations follows from the particular multiphase ISM model used there and the associated difficulty to accurately model the appropriate wave damping in the different phases of the ISM, as we lay out below.

In order for the CRs to escape the dense gas without significant hadronic losses, the diffusive time-scale $\tau_{\rm diff} \approx L^2/\kappa_\parallel$ needs to be smaller than the hadronic loss time $\tau_{\rm had} \approx 1/(n\sigma_{\rm pp}c)$, where L is the scale height of the disc, $\sigma_{\rm pp} \approx 25$ mbarn is the total inelastic proton–proton cross-section at kinetic proton energies of 1–3 GeV (Kafexhiu et al. 2014), and c is the light speed. By rearranging this inequality we derive a lower bound on the effective diffusion coefficient needed to allow the CRs to leave the galaxy

$$\kappa_\parallel > L^2 n\sigma_{\rm pp}c. \tag{5}$$

In the AURIGA model, the star-forming phase is governed by an equation of state (Springel & Hernquist 2003) resulting in a relatively smooth gas distribution where stars form at gas densities above $n_{\rm th} \sim 0.13$ cm^{-3}. This results in flat and extended gas discs in the AURIGA simulations (top panels of Fig. 3) of scale height $\sim$1.5 kpc (see vertical gas profiles in Fig. B1) with densities in the disc mid-plane of $n \lesssim 0.4$ cm^{-3} (cf. left-hand panels in Fig. 4). Using this density in equation (5) shows that for the AURIGA model a value of $\kappa_\parallel \gtrsim 10^{28}$ cm^2 s^{-1} allows CRs to escape.

On the other hand, in the FIRE-2 simulations the ISM is treated differently and allows for the formation of a multiphase ISM including a cool and dense phase with a significant amount of gas at densities $n \gtrsim 10$ cm^{-3} (see fig. 9 of Hopkins et al. 2020) in their $L_\star$ galaxies. For those densities and assuming similar gas disc scale heights, equation (5) results in $\kappa_\parallel \gtrsim 2 \times 10^{29}$ cm^2 s^{-1} in order to allow the CRs to escape efficiently from the ISM. Physically, ion-neutral damping would strongly damp the self-excited Alfvén waves so that CRs become weakly coupled to the largely neutral gas and could escape almost ballistically at their intrinsic speed of light from these regions (Wiener et al. 2017). Once they enter the warm-hot phase of the ISM, they couple again to the gas (because of the weaker wave damping processes such as non-linear Landau damping) so that they are transported at the Alfvén wave speed, which corresponds to an effective parallel diffusion coefficients in the MW today of $\kappa_\parallel = (1-3) \times 10^{28}$ cm^2 s^{-1}. A failure to model this transition results in a more diffusively transported CR gas in the warm-hot phases of the ISM and CGM (see also discussion in Salem, Bryan & Hummels 2014). It has been suggested by Farber et al. (2018) that the decoupling of CRs at low temperatures and high densities can be approximated by artificially increasing the diffusion coefficient in low-temperature gas by a factor of 30 in comparison to the general CGM gas (their equation 13). This work shows that with this simple decoupling mechanism CRs can efficiently escape the ISM and their dynamical effect is dramatically increased.

The strongest impact of CRs on the central galaxy we can find in our study is the reduction in size of the gaseous and stellar disc. Very similar results regarding the sizes of the stellar discs have been obtained by the FIRE-2 group (see e.g. their fig. 12 in Hopkins et al. 2020) who did not investigate the underlying reasons. Here, we find that the interplay of CRs and the wind feedback model on the scales of the gas disc mediates large-scale effects on the accretion flow of gas. In the CR runs, we observe more spherically symmetric outflows blocking the coherent gas accretion in the direction of the disc plane. This in turn modifies the angular momentum acquisition

of the galaxy and manifests itself in accretion of gas from a smaller region.

Our results are in stark contrast to the results from Salem et al. (2014) where the stellar disc grows in size when CRs are considered. The reason for this is not entirely clear but the very different feedback implementations and resolution effects might certainly play a role. These earlier results analysed simulations of worse resolution compared to the ones used here. Furthermore, the fiducial model used in that study results in a very compact stellar disc of unrealistic size. In contrast to this, the AURIGA-CR models start out from galactic discs of realistic size and mass because the wind feedback of the AURIGA noCR runs was tuned to reproduce MW-like galaxies. We discuss the uncertainties of the wind model in more detail in the next section.

6.4.2 Effects on the circumgalactic medium

The most noticeable effect of CRs in the AURIGA simulations is on the structure and morphology of the CGM. Whereas the overall baryonic mass in the CGM is not drastically effected (see density profiles in Fig. 10), the additional CR pressure affects the small-scale density and temperature distribution of the CGM. In particular our CRdiff model has a smoother and cooler CGM which is maintained by the additional CR pressure which smoothes out small-scale high density clumps in the CGM and supports the gas at lower temperatures against gravity. These findings are qualitatively similar to earlier results presented in the literature (e.g. Salem et al. 2014, 2016; Chen, Bryan & Salem 2016; Butsky & Quinn 2018).

The findings that the CGM becomes smoother and slightly cooler when diffusing CRs are included is consistent with the results of small-scale ISM simulations of the galactic disc using stratified boxes (Girichidis et al. 2016, 2018; Simpson et al. 2016). In particular, Girichidis et al. (2018) find that the CR pressure inside the disc ($z \lesssim$ 1 kpc) is largely in equilibrium with the thermal pressure as is the case for all our CR runs (compare Fig. 3). At distances larger than that ($z \gtrsim 1$ kpc), the CR pressure starts to dominate over the thermal pressure with values of $P_{\rm cr}/P_{\rm th} = 10$–100 in good agreement with our results. Thus, despite the approximations of our ISM model and the comparatively lower resolution results on the scales studied here, the simulations appear to be converged.

By contrast, our CRdiffalfven model shows a warmer CGM in comparison to the model without CRs (noCR) and in strong contrast to earlier work presented in the literature (e.g. Salem et al. 2014, 2016; Chen et al. 2016). As explained above, the reason is the additional CR Alfvén wave cooling term that emulates CR energy losses as they are resonantly exciting Alfvén waves which scatter their pitch angles (angle between their momentum and mean magnetic field vectors). This causes them to isotropise in the Alfvén wave frame and to stream with the Alfvén velocity along the local direction of the magnetic fields (Wiener et al. 2017). Whereas this approximation is justified as long as CR streaming and diffusion fluxes match each other, this cannot be guaranteed at all times due to the dispersive mathematical nature of the diffusion operator. Clearly more work is needed to confirm this finding and to better understand the final state of the CGM in the presence of streaming CRs. On the contrary, recent results by the FIRE-2 simulations suggest that CRs are able to reduce the CGM temperature from $\gtrsim$10^5 to $\sim$10^4 K (see fig. 7 in Ji et al. 2020) by providing enough pressure support. Our simulations do not support such a drastic change in CGM temperature as we have shown in Fig. 13. In fact, a complete suppression of the hot phase as in the FIRE-2 simulations is at odds with X-ray observations

of the MW hot halo ($\sim 10^6$ K, Fang, Bullock & Boylan-Kolchin 2013; Faerman, Sternberg & McKee 2017).

The most likely reason for this is the implementation of feedback in FIRE-2, which is very explosive and could cause a quenching of their magnetic dynamo. This yields to saturation at a low level with a magnetic energy density that is a factor of 100 below our results. Note that our magnetic field distribution matches Faraday rotation measure data of the MW and external galaxies (Pakmor et al. 2018). The lower magnetic field strength causes the Alfvén speed $\boldsymbol{v}_A = \boldsymbol{B}/\sqrt{4\pi\rho}$ to be ten times smaller and hence, also reduces the CR Alfvén wave cooling rate, $|\boldsymbol{v}_A \cdot \boldsymbol{\nabla} P_{\mathrm{cr}}|$, by the same factor. Hence, the FIRE-2 runs represent an extreme version of our CRdiff model, in which the CR Alfvén wave cooling is nearly absent.

6.5 Modelling uncertainties

The results obtained in this paper are subject to a number of physical modelling uncertainties which we discuss below.

6.5.1 The AURIGA feedback model

In this study, CRs are modelled on top of the AURIGA galaxy formation model which has been calibrated to reproduce MW-like galaxies without the inclusion of CRs. We have kept any 'free' parameter in the sub-grid model as in the AURIGA model and added the CR physics on top of this. Therefore, the comparably small impact of CR physics on global galaxy properties such as the total stellar mass or SFR (as opposed to previous findings where CRs showed strong impacts) might be due to the already efficient feedback implementation of the AURIGA model without CRs. Here, the biggest uncertainty is the effect of the wind model coupled with the CR feedback. In the AURIGA model, the details of the wind model are calibrated to reproduce observed galaxy properties without the additional effects of CRs. In this study, we add CR feedback on top of the already calibrated feedback model of AURIGA without re-tuning any parameters. Whereas this strategy allows us to cleanly single out the effects of CRs, one could imagine that the calibrated AURIGA model might already account for some of the effects CRs might have on galaxy formation. Therefore, the exact choice of parameters for the wind model in combination with the effects of CRs might change the amount of angular momentum losses as observed in our study. There might exist a different combination of wind model parameters and CR feedback model in which the CGM flow is less affected by the CRs and thus the angular momentum losses are reduced. However, the cause of the different angular momentum build-up in the three CRs variants is the modified morphology of the disc–halo interface and we expect the basic effects to be robust. Nevertheless, unless the parameters of the wind model are derived from either observations or theoretical considerations the wind model presents a considerable systematic uncertainty.

6.5.2 The ISM model

Our simulations adopt a pressurized ISM which even in the stellar disc is relatively smooth without high density, low-temperature peaks (e.g. Marinacci et al. 2019, figs 9 and 10). Similarly to the AURIGA feedback model we have not re-tuned any of the parameters of the multiphase model for star formation. This is justified because all our models still reproduce the Kennicutt–Schmidt relation (Kennicutt 1998) against which this model was calibrated and we have explicitly checked that each of the models reproduces the normalization and

slope of the observed relation. Additionally, it is not entirely clear how CRs could be included in the Springel and Hernquist model in the first place, so that for the purposes of this study it appears most adequate to not modify parameters of the subgrid model.

Transforming to a multiphase ISM will affect how CRs escape dense star-forming regions and thus how they impact the dynamics of the ISM. Most importantly, recent modelling of CR data suggests that CRs below 200 GeV that carry most of the CR pressure are streaming with the Alfvén velocity and are diffusively transported at higher energies (Evoli et al. 2018). Hence, we need to model CR streaming in the self-confinement picture where CRs resonantly excite Alfvén waves to accurately model their transport in galaxies and the CGM using the two-moment method (Thomas & Pfrommer 2019). Following the evolution equation of small-scale resonant Alfvén wave energies provides a means to self-consistently model CR diffusion in the Alfvén wave frame. This will enable us to simultaneously account for the weaker coupling of CRs in the cold phase ($T < 10^4$ K) due to increased ion-neutral damping and the stronger dynamical coupling in the warm-hot phases due to the prevalent non-linear Landau damping (e.g. McKenzie & Bond 1983) and turbulent damping processes (e.g. Farmer & Goldreich 2004; Yan & Lazarian 2004).

6.5.3 The CR transport models

Another fundamental uncertainty is given by the details of the CR transport physics and its numerical implementation. To explore the influence of CR transport on galaxy formation we decided to adopt three different variants of CR transport and focused our analysis on the question of how each variant impacts the stellar and gaseous properties. These models result in qualitatively similar global trends, but show that structural properties differ between each of the CR variants. As expected, our CRdiffalfven model that emulates CR streaming gave the most realistic results in terms of stellar and gaseous disc properties as well as for the CGM in agreement with recent findings by Butsky & Quinn (2018). In particular, the resulting gamma-ray emission (see Fig. 14) appeared to be an important discriminant of the studied CR models.

6.5.4 Cosmological variance of accretion histories

In this study, we have focused on analysing the effects of CR physics in cosmological simulations. Additionally to the different CR transport physics the two galaxies in these kind of simulations are further affected by the different accretion histories. For example, AuL8 undergoes a major merger at a lookback time of $\sim$6 Gyr whereas Au6 has a very quiet merger history at low redshift. Thus, there are natural differences in the evolution and properties between the two haloes complicating the separation of the effects of CRs and cosmological accretion history. On the other hand, CRs do not only affect the main galaxy but also the merging satellites and thus a complete picture of their effects can only be gained by studying a large cosmological volume, which samples the complete galaxy population.

6.5.5 Numerical resolution study

Convergence of galaxy properties across different levels of numerical resolution is difficult to achieve in galaxy formation simulations and poses an additional challenge in understanding the physics of galaxy formation. Ideally, the outcome of a simulation should only depend

on the modelled physics and not on numerical resolution. In section 6 of Grand et al. (2017) it has been shown that our baseline model, the AURIGA model without CRs, is numerically well converged. We have run additional eight simulations with a factor of 8 and 16 lower in mass resolution in order to test the numerical robustness of our results. While we detail the resolution dependence of our results in Appendix D, here we summarize the main results: stellar and halo masses of the central galaxies are well converged across different resolution levels (see Table D1) and we have verified that all our results and conclusions do not depend on resolution. Especially our main findings are numerically converged: those include the more compact stellar discs (see Fig. D2 in the Appendix) mediated by the modified accretion flow in the CR runs as well as the gas discs inflated by CR pressure and the smoother CGM in the CRadv and CRdiff models in comparison to the other two models (cf. Fig. D1 and the upper row of Fig. 9). Thus, our simulations are well suited to study the effects of CRs in cosmological simulations as the evolution of the galaxies only depends on our physical modelling and not on numerical resolution.

7 CONCLUSIONS

In this work, we set out to study the effects of CRs on the formation of MW-like galaxies in a cosmological context. To this extend we have performed eight magnetohydrodynamical simulations in the context of the AURIGA project (Grand et al. 2017) with three different models of varying complexity for the physics of CR transport. All simulations are performed with the second-order accurate moving mesh code Arepo (Springel 2010; Pakmor et al. 2016a) for magnetohydrodynamics. The galaxy formation model includes detailed models for gas cooling and heating, star formation as well as stellar and AGN feedback. Additionally, the simulations include the following CR physics: the simplest model advects CRs with the gas flow (CRadv), a more complex variant additionally follows the anisotropic diffusion of CRs parallel to the magnetic field (CRdiff) while in the most complex model CRs are further allowed to cool via the excitation of Alfvén waves (CRdiffalfven), attempting to emulate the transport process of self-confined CR streaming.

We have studied in detail the properties of the central galaxy and the CGM and compared model predictions from the CR runs to the fiducial AURIGA model. Bulk galaxy properties are only weakly affected by CRs, whereas the morphology and angular momentum distribution of our galaxies as well as the properties of the CGM are sensitive to the details of the CR physics implementation. Our conclusions are summarized as follows:

(i) Galaxy properties like the total stellar mass, SFR, or gas mass are largely unaffected by CRs and stable across different physics variants. While previous works have found that CRs are able to suppress star formation in isolated galaxy simulations, our cosmological simulations show that the SFR is largely unaffected by CR feedback (see Fig. 2). Note that this could be partially due to the already efficient feedback in AURIGA, which can in principle mask some of the feedback effects CRs would otherwise have.

(ii) Comparing structural parameters of the galaxies such as disc sizes, disc-to-total stellar mass ratios, or gas disc morphology we find strong differences between the simulations that include CRs and the fiducial AURIGA model. The CRadv and CRdiff models result in more compact, bulge dominated discs which show thicker and smoother gas discs, in which the vertical force balance is dominated by the CR pressure (see e.g. Figs 1 and 3). A similar reduction of stellar disc size is also found by the FIRE-2 group in their simulations

including CR feedback. In contrast, the stellar and gaseous discs in the CRdiffalfven model have disc sizes which lie between the fiducial results and the more extreme CR models (e.g. the left-hand panel of Fig. 4). We find that the magnetic field strength and morphology is similar in all our runs with a value of the order of $\sim$10 µG (that is consistent with MW observations, see Pakmor et al. 2018) so that our magnetic energy density is roughly 100 times larger than those obtained with the FIRE-2 simulations (e.g. figs 3 and 19 of Hopkins et al. 2020).

(iii) The interplay of CRs and the wind feedback model strongly affects the gas flow patterns in the CGM (Figs 6 and 7). The more compact, bulge dominated discs in the CR simulations cause the outflows to become more spherically symmetric in comparison to the fiducial AURIGA run (Fig. 6) and thus alter the angular momentum acquisition in the cosmological runs. In this way, the action of CR feedback in the star-forming disc changes the outflow geometry and suppresses the baryonic accretion of high angular momentum gas, especially at late cosmic times (Fig. 5). As a consequence, the gas discs in the CR runs are smaller in size as is highlighted in the left-hand panels of Fig. 4.

(iv) On larger scales, CRs strongly affect the properties of the CGM. The advection and diffusion models exhibit a smoother and partly cooler CGM (Figs 9 and 10) where the additional CR pressure is able to stabilize the CGM against gravitational collapse compensating for the missing thermal pressure support at lower CGM temperatures. These runs therefore show large ($R \sim 50$ kpc) CR pressure contributions in the haloes. In contrast, the Alfvén wave model is only CR pressure dominated at the disc–halo interface and the CRs come into equilibrium with the thermal pressure as they are advected into the halo along stream lines of the galactic winds (see also Fig. 12). As CRs are actively transported across an effective scale height, they quickly cool, which greatly suppresses further turbulent mixing and causes a highly structured CR pressure distribution in the CGM (Fig. 9). This in turn causes a structured density and temperature distribution in the CGM, which maintains large volumes at thermally unstable temperatures of 10^5 K (Fig. 13) which is warmer than the cool ($\sim$$10^4$–$10^5$ K) CGM gas found in the CR FIRE-2 simulations (see fig. 7 in Ji et al. 2020).

(v) The magnetic and CR pressures trace each other within a factor of 5 out to the virial radius (Fig. 12). This implies that there is not enough free energy available to drive the hybrid, non-resonant CR instability (Bell 2004), which would require the CR-to-magnetic energy density ratio to be larger than $2c/v_d \sim 10^3$–10^4 where v_d is the drift speed of CRs that is close to the Alfvén speed. Excitation of the Bell instability would imply fast CR scattering, a much reduced CR diffusion coefficient by about seven orders of magnitudes and effectively transition to the CRadv model.

(vi) There are active ongoing efforts in developing efficient and accurate CR magnetohydrodynamical schemes (Jiang & Oh 2018; Thomas & Pfrommer 2019) to compute the CR feedback effects in cosmological simulations. To this end, direct observables are invaluable in constraining effective CR transport models, provided the approximations used for CR transport and the ISM are commensurate and not inconsistent. In Fig. 14, we compare the gamma-ray luminosity from hadronic CR interactions with the ISM of our models to observations of local galaxies. We find that the CRdiffalfven run agrees well with observed relations whereas the CRdiff and CRadv produce higher gamma-ray luminosities at the MW mass scale compared to observations. Our comparison here presents a first step towards understanding the effects of CRs on cosmological galaxy formation, but further work in this direction is needed to constrain valid CR transport coefficient and prevailing transport processes.

DATA AVAILABILITY

The data underlying this article will be shared on reasonable request to the corresponding author.

REFERENCES

Ackermann M. et al., 2012, Phys. Rev. Lett., 108, 011103
Amato E., Blasi P., 2018, Adv. Space Res., 62, 2731
Battaglia N., Bond J. R., Pfrommer C., Sievers J. L., 2012a, ApJ, 758, 74
Battaglia N., Bond J. R., Pfrommer C., Sievers J. L., 2012b, ApJ, 758, 75
Battaglia N., Bond J. R., Pfrommer C., Sievers J. L., 2013, ApJ, 777, 123
Beck R., Chamandy L., Elson E., Blackman E. G., 2019, Galaxies, 8, 4
Bell E. F., 2003, ApJ, 586, 794
Bell A. R., 2004, MNRAS, 353, 550
Blandford R., Eichler D., 1987, Phys. Rep., 154, 1
Bondi H., 1952, MNRAS, 112, 195
Bondi H., Hoyle F., 1944, MNRAS, 104, 273
Booth C. M., Agertz O., Kravtsov A. V., Gnedin N. Y., 2013, ApJ, 777, L16
Boulares A., Cox D. P., 1990, ApJ, 365, 544
Breitschwerdt D., McKenzie J. F., Voelk H. J., 1991, A&A, 245, 79
Breitschwerdt D., Dogiel V. A., Völk H. J., 2002, A&A, 385, 216
Brook C. B., Stinson G., Gibson B. K., Wadsley J., Quinn T., 2012, MNRAS, 424, 1275
Buck T., Dutton A. A., Macciò A. V., 2019, MNRAS, 486, 1481
Buck T., Obreja A., Macciò A. V., Minchev I., Dutton A. A., Ostriker J. P., 2020, MNRAS, 491, 3461
Butsky I. S., Quinn T. R., 2018, ApJ, 868, 108
Cerri S. S., Gaggero D., Vittino A., Evoli C., Grasso D., 2017, J. Cosmol. Astropart. Phys., 2017, 019
Chabrier G., 2003, PASP, 115, 763
Chan T. K., Kereš D., Hopkins P. F., Quataert E., Su K.-Y., Hayward C. C., Faucher-Giguère C.-A., 2019, MNRAS, 488, 3716
Chen J., Bryan G. L., Salem M., 2016, MNRAS, 460, 3335
Chomiuk L., Povich M. S., 2011, AJ, 142, 197
Crain R. A., McCarthy I. G., Frenk C. S., Theuns T., Schaye J., 2010, MNRAS, 407, 1403
Cummings A. C. et al., 2016, ApJ, 831, 18
Davé R., Anglés-Alcázar D., Narayanan D., Li Q., Rafieferantsoa M. H., Appleby S., 2019, MNRAS, 486, 2827
Di Matteo T., Springel V., Hernquist L., 2005, Nature, 433, 604
Dolag K., Komatsu E., Sunyaev R., 2016, MNRAS, 463, 1797
Dorfi E. A., Breitschwerdt D., 2012, A&A, 540, A77
Dubois Y., Peirani S., Pichon C., Devriendt J., Gavazzi R., Welker C., Volonteri M., 2016, MNRAS, 463, 3948
Ehlert K., Weinberger R., Pfrommer C., Pakmor R., Springel V., 2018, MNRAS, 481, 2878
Emerick A., Bryan G. L., Mac Low M.-M., 2018, ApJ, 865, L22
Enßlin T. A., Pfrommer C., Springel V., Jubelgas M., 2007, A&A, 473, 41
Enßlin T., Pfrommer C., Miniati F., Subramanian K., 2011, A&A, 527, A99
Everett J. E., Zweibel E. G., Benjamin R. A., McCammon D., Rocks L., Gallagher J. S. III, 2008, ApJ, 674, 258
Evoli C., Gaggero D., Vittino A., Di Bernardo G., Di Mauro M., Ligorini A., Ullio P., Grasso D., 2017, J. Cosmol. Astropart. Phys., 2017, 015

Evoli C., Blasi P., Morlino G., Aloisio R., 2018, Phys. Rev. Lett., 121, 021102
Evoli C., Aloisio R., Blasi P., 2019, Phys. Rev. D, 99, 103023
Evoli C., Morlino G., Blasi P., Aloisio R., 2020, Phys. Rev. D, 101, 023013
Faerman Y., Sternberg A., McKee C. F., 2017, ApJ, 835, 52
Fang T., Bullock J., Boylan-Kolchin M., 2013, ApJ, 762, 20
Farber R., Ruszkowski M., Yang H. Y. K., Zweibel E. G., 2018, ApJ, 856, 112
Farmer A. J., Goldreich P., 2004, ApJ, 604, 671
Faucher-Giguère C.-A., Lidz A., Zaldarriaga M., Hernquist L., 2009, ApJ, 703, 1416
Gaspari M., Ruszkowski M., Oh S. P., 2013, MNRAS, 432, 3401
Genel S., Vogelsberger M., Nelson D., Sijacki D., Springel V., Hernquist L., 2013, MNRAS, 435, 1426
Girichidis P. et al., 2016, ApJ, 816, L19
Girichidis P., Naab T., Hanasz M., Walch S., 2018, MNRAS, 479, 3042
Grand R. J. J. et al., 2017, MNRAS, 467, 179
Grand R. J. J. et al., 2019, MNRAS, 490, 4786
Griffin R. D., Dai X., Thompson T. A., 2016, ApJ, 823, L17
Guo F., Oh S. P., 2008, MNRAS, 384, 251
Hanasz M., Lesch H., 2003, A&A, 412, 331
Hanasz M., Lesch H., Naab T., Gawryszczak A., Kowalik K., Wóltański D., 2013, ApJ, 777, L38
Harris J., Zaritsky D., 2009, AJ, 138, 1243
Haverkorn M., 2015, Magnetic Fields in the Milky Way. Springer-Verlag, Berlin Heidelberg, p. 483
Haverkorn M., Gaensler B. M., Brown J. A. C., McClure-Griffiths N. M., Dickey J. M., Green A. J., 2006, Astron. Nachr., 327, 483
Henriques B. M. B., White S. D. M., Thomas P. A., Angulo R., Guo Q., Lemson G., Springel V., Overzier R., 2015, MNRAS, 451, 2663
Hopkins P. F. et al., 2018, MNRAS, 480, 800
Hopkins P. F. et al., 2020, MNRAS, 492, 3465
Hunter J. D., 2007, Comput. Sci. Eng., 9, 90
Ipavich F. M., 1975, ApJ, 196, 107
Jacob S., Pfrommer C., 2017a, MNRAS, 467, 1449
Jacob S., Pfrommer C., 2017b, MNRAS, 467, 1478
Jacob S., Pakmor R., Simpson C. M., Springel V., Pfrommer C., 2018, MNRAS, 475, 570
Ji S. et al., 2020, MNRAS, 496, 4221
Jiang Y.-F., Oh S. P., 2018, ApJ, 854, 5
Jóhannesson G., Porter T. A., Moskalenko I. V., 2019, ApJ, 879, 91
Jones E., Oliphant T., Peterson P. et al., 2001, SciPy: Open source scientific tools for Python. http://www.scipy.org/
Jubelgas M., Springel V., Enßlin T., Pfrommer C., 2008, A&A, 481, 33
Kafexhiu E., Aharonian F., Taylor A. M., Vila G. S., 2014, Phys. Rev. D, 90, 123014
Karakas A. I., 2010, MNRAS, 403, 1413
Kaviraj S. et al., 2017, MNRAS, 467, 4739
Kennicutt R. C., Jr, 1998, ARA&A, 36, 189
Kluyver T. et al., 2016, in Loizides F., Schmidt B., eds, Positioning and Power in Academic Publishing: Players, Agents and Agendas. IOS Press, p. 87
Kravtsov A. V., Borgani S., 2012, ARA&A, 50, 353
Krumholz M. R., Thompson T. A., 2012, ApJ, 760, 155
Kulsrud R., Pearce W. P., 1969, ApJ, 156, 445
Lacki B. C., Thompson T. A., Quataert E., Loeb A., Waxman E., 2011, ApJ, 734, 107
Licquia T. C., Newman J. A., 2015, ApJ, 806, 96
Lipari P., 2014, preprint (arXiv:1407.5223)
Loewenstein M., Zweibel E. G., Begelman M. C., 1991, ApJ, 377, 392
Marinacci F., Pakmor R., Springel V., 2014, MNRAS, 437, 1750
Marinacci F., Sales L. V., Vogelsberger M., Torrey P., Springel V., 2019, MNRAS, 489, 4233
McCarthy I. G., Le Brun A. M. C., Schaye J., Holder G. P., 2014, MNRAS, 440, 3645
McCarthy I. G., Schaye J., Bird S., Le Brun A. M. C., 2017, MNRAS, 465, 2936
McKenzie J. F., Bond R. A. B., 1983, A&A, 123, 111
McNamara B. R., Nulsen P. E. J., 2007, ARA&A, 45, 117
Mignone A., Bodo G., Vaidya B., Mattia G., 2018, ApJ, 859, 13

Mihalas D., Mihalas B. W., 1984, Foundations of Radiation Hydrodynamics. Oxford Univ. Press, New York
Miniati F., Ryu D., Kang H., Jones T. W., 2001, ApJ, 559, 59
Moster B. P., Naab T., White S. D. M., 2013, MNRAS, 428, 3121
Murray N., Quataert E., Thompson T. A., 2005, ApJ, 618, 569
Oppenheimer B. D., Davé R., 2006, MNRAS, 373, 1265
Pakmor R., Springel V., 2013, MNRAS, 432, 176
Pakmor R., Bauer A., Springel V., 2011, MNRAS, 418, 1392
Pakmor R., Springel V., Bauer A., Mocz P., Munoz D. J., Ohlmann S. T., Schaal K., Zhu C., 2016a, MNRAS, 455, 1134
Pakmor R., Pfrommer C., Simpson C. M., Kannan R., Springel V., 2016b, MNRAS, 462, 2603
Pakmor R., Pfrommer C., Simpson C. M., Springel V., 2016c, ApJ, 824, L30
Pakmor R., Guillet T., Pfrommer C., Gómez F. A., Grand R. J. J., Marinacci F., Simpson C. M., Springel V., 2018, MNRAS, 481, 4410
Pakmor R. et al., 2019, preprint (arXiv:1911.11163)
Peng F.-K., Wang X.-Y., Liu R.-Y., Tang Q.-W., Wang J.-F., 2016, ApJ, 821, L20
Pérez F., Granger B. E., 2007, Comput. Sci. Eng., 9, 21
Peterson J. R., Fabian A. C., 2006, Phys. Rep., 427, 1
Pfrommer C., 2013, ApJ, 779, 10
Pfrommer C., Enßlin T. A., 2004, A&A, 413, 17
Pfrommer C., Springel V., Enßlin T. A., Jubelgas M., 2006, MNRAS, 367, 113
Pfrommer C., Pakmor R., Schaal K., Simpson C. M., Springel V., 2017a, MNRAS, 465, 4500
Pfrommer C., Pakmor R., Simpson C. M., Springel V., 2017b, ApJ, 847, L13
Pillepich A. et al., 2018, MNRAS, 473, 4077
Porter T. A., Jóhannesson G., Moskalenko I. V., 2017, ApJ, 846, 67
Portinari L., Chiosi C., Bressan A., 1998, A&A, 334, 505
Powell K. G., Roe P. L., Linde T. J., Gombosi T. I., De Zeeuw D. L., 1999, J. Comput. Phys., 154, 284
Ptuskin V. S., Voelk H. J., Zirakashvili V. N., Breitschwerdt D., 1997, A&A, 321, 434
Ptuskin V. S., Moskalenko I. V., Jones F. C., Strong A. W., Zirakashvili V. N., 2006, ApJ, 642, 902
Puchwein E., Springel V., 2013, MNRAS, 428, 2966
Rahmani S., Lianou S., Barmby P., 2016, MNRAS, 456, 4128
Rojas-Bravo C., Araya M., 2016, MNRAS, 463, 1068
Rosdahl J., Schaye J., Teyssier R., Agertz O., 2015, MNRAS, 451, 34
Ruszkowski M., Yang H.-Y. K., Zweibel E., 2017a, ApJ, 834, 208
Ruszkowski M., Yang H. Y. K., Reynolds C. S., 2017b, ApJ, 844, 13
Salem M., Bryan G. L., 2014, MNRAS, 437, 3312
Salem M., Bryan G. L., Hummels C., 2014, ApJ, 797, L18
Salem M., Bryan G. L., Corlies L., 2016, MNRAS, 456, 582
Samui S., Subramanian K., Srianand R., 2010, MNRAS, 402, 2778
Sawala T. et al., 2016, MNRAS, 457, 1931
Schaye J., Dalla Vecchia C., 2008, MNRAS, 383, 1210
Schaye J. et al., 2015, MNRAS, 446, 521
Sérsic J. L., 1963, BAAA, 6, 41
Sijacki D., Pfrommer C., Springel V., Enßlin T. A., 2008, MNRAS, 387, 1403
Simpson J. A., Garcia-Munoz M., 1988, Space Sci. Rev., 46, 205
Simpson C. M., Pakmor R., Marinacci F., Pfrommer C., Springel V., Glover S. C. O., Clark P. C., Smith R. J., 2016, ApJ, 827, L29
Socrates A., Davis S. W., Ramirez-Ruiz E., 2008, ApJ, 687, 202

Springel V., 2010, MNRAS, 401, 791
Springel V., Hernquist L., 2003, MNRAS, 339, 289
Springel V. et al., 2005, Nature, 435, 629
Stinson G. S., Brook C., Macciò A. V., Wadsley J., Quinn T. R., Couchman H. M. P., 2013, MNRAS, 428, 129
Strong A. W., Moskalenko I. V., 1998, ApJ, 509, 212
Sun X. H., Reich W., 2012, A&A, 543, A127
Tabatabaei F. S. et al., 2013, A&A, 552, A19
Tang Q.-W., Wang X.-Y., Tam P.-H. T., 2014, ApJ, 794, 26
Thielemann F.-K. et al., 2003, Nucl. Phys. A, 718, 139
Thomas T., Pfrommer C., 2019, MNRAS, 485, 2977
Thomas T., Pfrommer C., Enßlin T., 2020, ApJ, 890, L18
Thompson T. A., Quataert E., Murray N., 2005, ApJ, 630, 167
Travaglio C., Hillebrandt W., Reinecke M., Thielemann F.-K., 2004, A&A, 425, 1029
Tumlinson J. et al., 2013, ApJ, 777, 59
Uhlig M., Pfrommer C., Sharma M., Nath B. B., Enßlin T. A., Springel V., 2012, MNRAS, 423, 2374
van de Voort F., Springel V., Mandelker N., van den Bosch F. C., Pakmor R., 2019, MNRAS, 482, L85
Vogelsberger M., Genel S., Sijacki D., Torrey P., Springel V., Hernquist L., 2013, MNRAS, 436, 3031
Vogelsberger M. et al., 2014, MNRAS, 444, 1518
Walt S. v. d., Colbert S. C., Varoquaux G., 2011, Comput. Sci. Eng., 13, 22
Wang L., Dutton A. A., Stinson G. S., Macciò A. V., Penzo C., Kang X., Keller B. W., Wadsley J., 2015, MNRAS, 454, 83
Webber W. R., 1998, ApJ, 506, 329
Weinberger R. et al., 2017, MNRAS, 465, 3291
Wiener J., Oh S. P., Guo F., 2013, MNRAS, 434, 2209
Wiener J., Pfrommer C., Oh S. P., 2017, MNRAS, 467, 906
Wilke K., Klaas U., Lemke D., Mattila K., Stickel M., Haas M., 2004, A&A, 414, 69
Yan H., Lazarian A., 2004, ApJ, 614, 757
Zhang Y., Peng F.-K., Wang X.-Y., 2019, ApJ, 874, 173
Zhuravleva I. et al., 2014, Nature, 515, 85
Zirakashvili V. N., Breitschwerdt D., Ptuskin V. S., Voelk H. J., 1996, A&A, 311, 113
Zweibel E. G., 2017, Phys. Plasmas, 24, 055402

APPENDIX A: SURFACE DENSITY FITS

In Fig. A1, we show azimuthally averaged surface density fits to the stellar disc of the eight simulations at redshift $z = 0$. Surface density profiles are created for all the stellar mass within ± 5 kpc of the mid-plane in the vertical direction. The profiles are simultaneously fit with a Sérsic (1963) (red dashed curve) and exponential (blue curve) profile using a non-linear least-squares method. Resulting fit values for the disc scale length, $R_{\rm d}$, the bulge effective radius, $R_{\rm eff}$, and the bulge Sérsic index, n, are given in each panel. This figure shows that the CRadv and CRdiff runs result in more compact bulge-dominated galaxies whereas the CRdiffalfven run results in a disc-dominated galaxy more similar to the fiducial AURIGA run. From the fits we derive disc-to-total mass ratios (D/T) which are given in Table 1 in the main text.
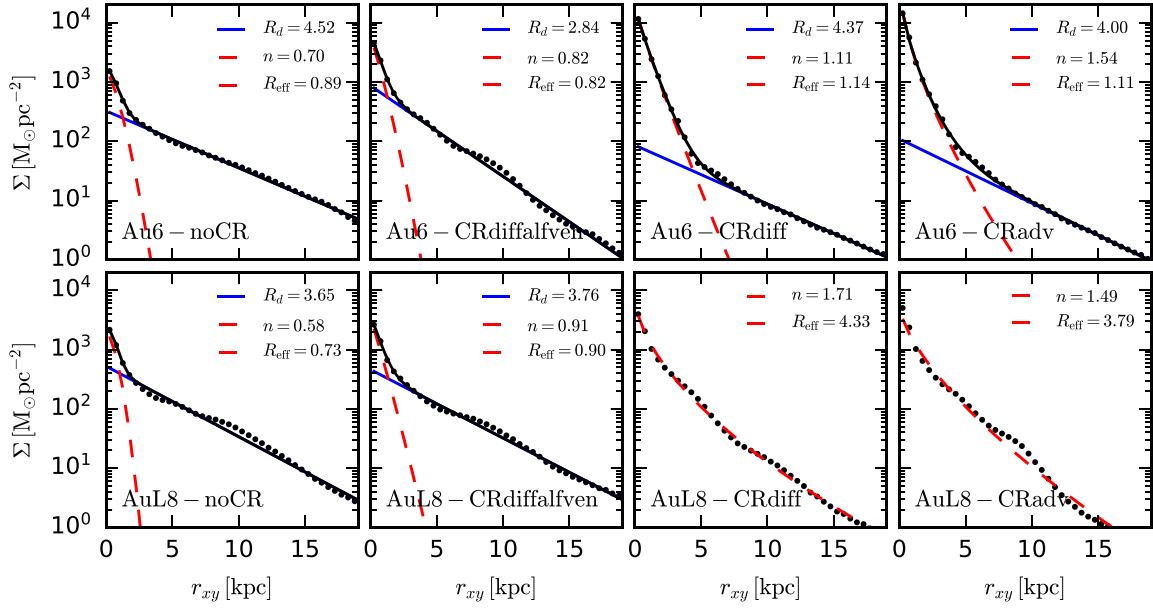
Figure A1. Face-on stellar surface density profiles for all simulations at $z = 0$ (black dots). The four models of Au6 are shown in the upper row, AuL8 in the bottom row. The profiles are simultaneously fit with a Sérsic (1963) (red dashed curve) and exponential (blue curve) profile. The total fitted profile is indicated by the black curve. Resulting fit values for the disc scale length, R_d, the bulge effective radius, R_{eff}, and the bulge Sérsic index, n, are given in each panel. The CRdiff and CRadv models of AuL8 are well fitted by a pure Sérsic profile.

APPENDIX B: VERTICAL PROFILES

We have created vertical profiles similar to the radial profiles shown in Fig. 4 for the gas density, the magnetic field strength, the CR pressure, and the gas thermal pressure in the central galaxy. We select all Voronoi cells in a cylinder of radius $r = 30$ kpc and height $z = \pm 10$ kpc and show the data in 30 bins linearly spaced in z in Fig. B1.
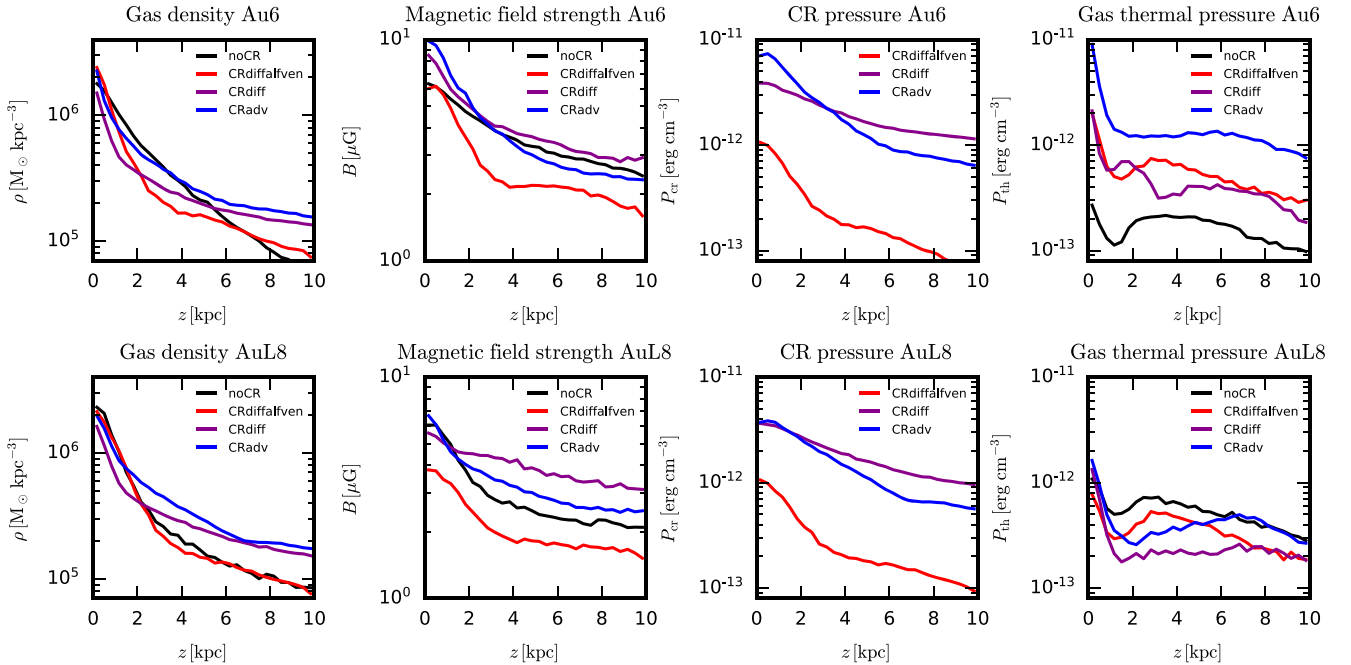

Figure B1. Vertical profiles of the gas density (left-hand panel), magnetic field strength (second panel), CR pressure (third panel), and gas thermal pressure (fourth panel) for the four models of Au6 in the upper row and AuL8 in the lower row.

APPENDIX C: ANGULAR MOMENTUM DISTRIBUTION

Fig. C1 shows the distribution of gas angular momentum at eight different points in time for the tracer particles ending up in stars at present day. This highlights how the angular momentum of the accreted gas changes over time for the different CR runs compared to the noCR run. Upper panels show galaxy Au6 and lower panels AuL8, respectively. At early cosmic times ($t_{\mathrm{lookback}} \gtrsim 12$ Gyr, yellow colors) all simulations show a symmetric distribution of specific angular momenta around $l_z = 0$ kpc km s^{-1}. Then, at lookback times of about 8 Gyr (greenish colours) all runs have accreted gas with higher angular momentum of values $l_z \sim 1.5 \times 10^3$ kpc km s^{-1}. The noCR and the CRdiffalfven runs keep acquiring high angular momentum gas also at low redshift (smaller lookback times, blue colours) whereas the angular momentum gain in the CRdiff and CRadv runs is suppressed. Thus, at redshift zero, the angular momentum distribution in the latter cases peaks around $l_z \sim 1 \times 10^3$ kpc km s^{-1} and at $l_z \gtrsim 2 \times 10^3$ kpc km s^{-1} in the former cases (see vertical thin lines).

APPENDIX D: RESOLUTION STUDY

Our study shows that CRs strongly affect the CGM and the gaseous and stellar properties of the galactic discs. In combination with the model for the wind feedback, this results in a more hydrostatic gas halo and a modification of the gas accretion on to the central galaxy. This effect is already present at resolution levels 5 and 6 (at a factor of 8 and 16 lower in mass resolution, corresponding to $m_{\mathrm{dm}} = 2 \times 10^6$ M$_\odot$, $m_{\mathrm{b}} = 4 \times 10^5$ M$_\odot$, $\epsilon = 738$ pc and $m_{\mathrm{dm}} = 2 \times 10^7$ M$_\odot$, $m_{\mathrm{b}} = 3 \times 10^6$ M$_\odot$, $\epsilon = 1476$ pc) and does not change at our fiducial resolution at level 4 ($m_{\mathrm{dm}} = 3 \times 10^5$ M$_\odot$, $m_{\mathrm{b}} = 5 \times 10^4$ M$_\odot$, $\epsilon = 369$ pc).

We would like to emphasize that we do not change any subgrid parameters for the ISM, wind feedback, and CR physics when we change the numerical resolution. Hence, we do not expect to resolve new physics with increasing resolution but we aim at better resolving the poorly resolved regions at the disc–halo interface and the gas accretion and flow pattern in the CGM (i.e. we study convergence of our numerical model). For example, Fig. D1 shows the gas surface density maps of the four models at resolution level 5. These are the
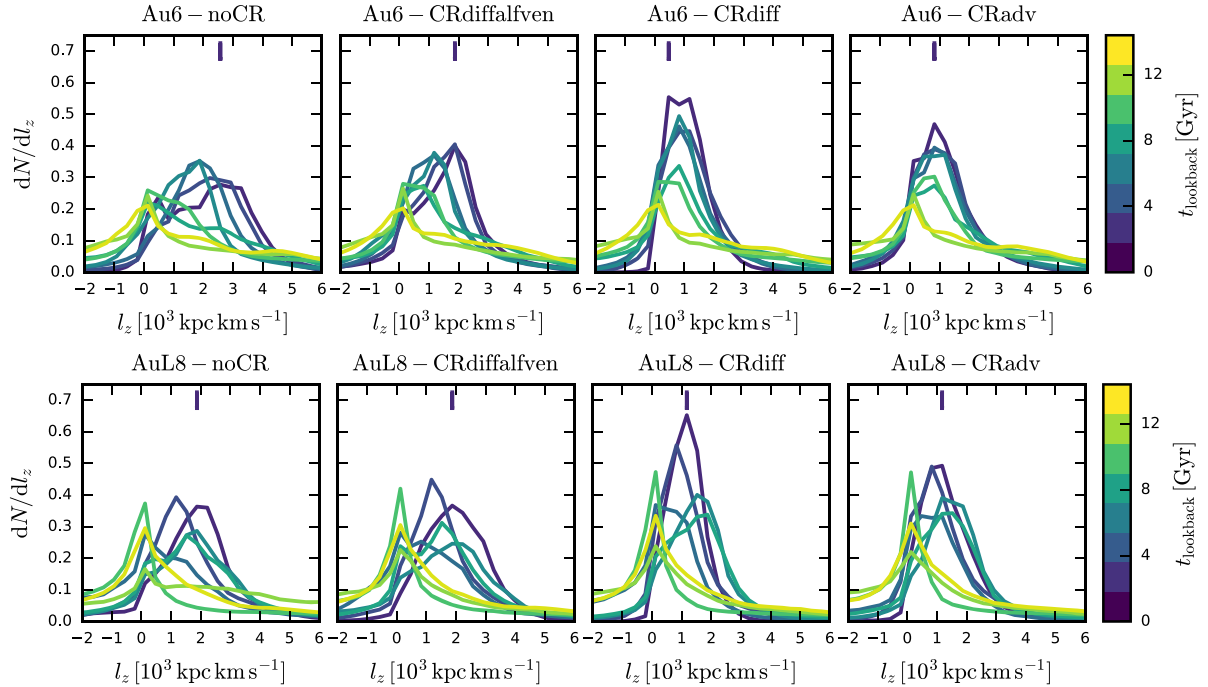

Figure C1. Normalized distribution functions of the gas' specific angular momentum for different lookback times as indicated with the colourbar on the right. Upper panels show results for the four different physics variants of Au6 and lower panels for AuL8, respectively. The vertical blue line indicates the maximum of the redshift zero distribution.
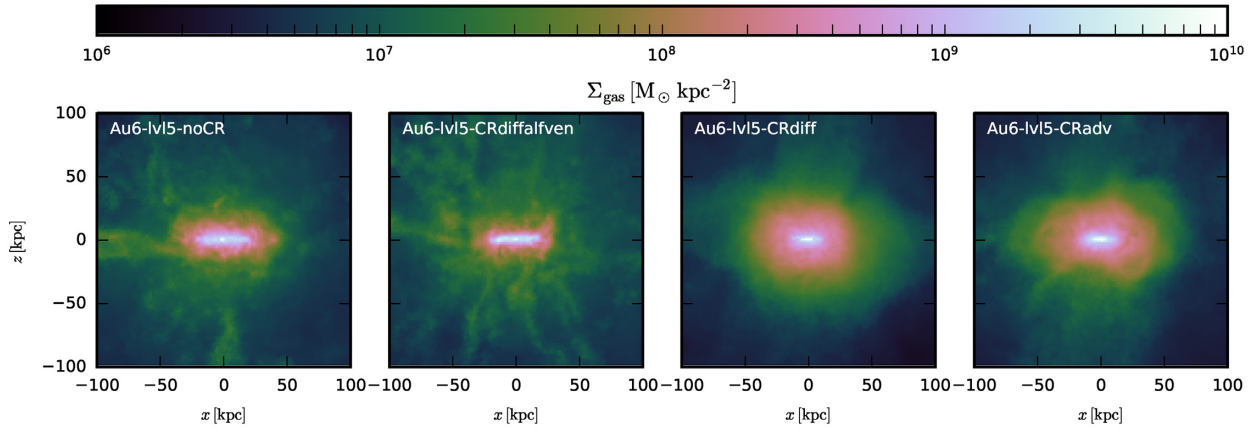
Figure D1. Gas surface density maps of Au6 level 5 for all four models as indicated in the panels. Orientation and projection depth are as in Fig. 9.
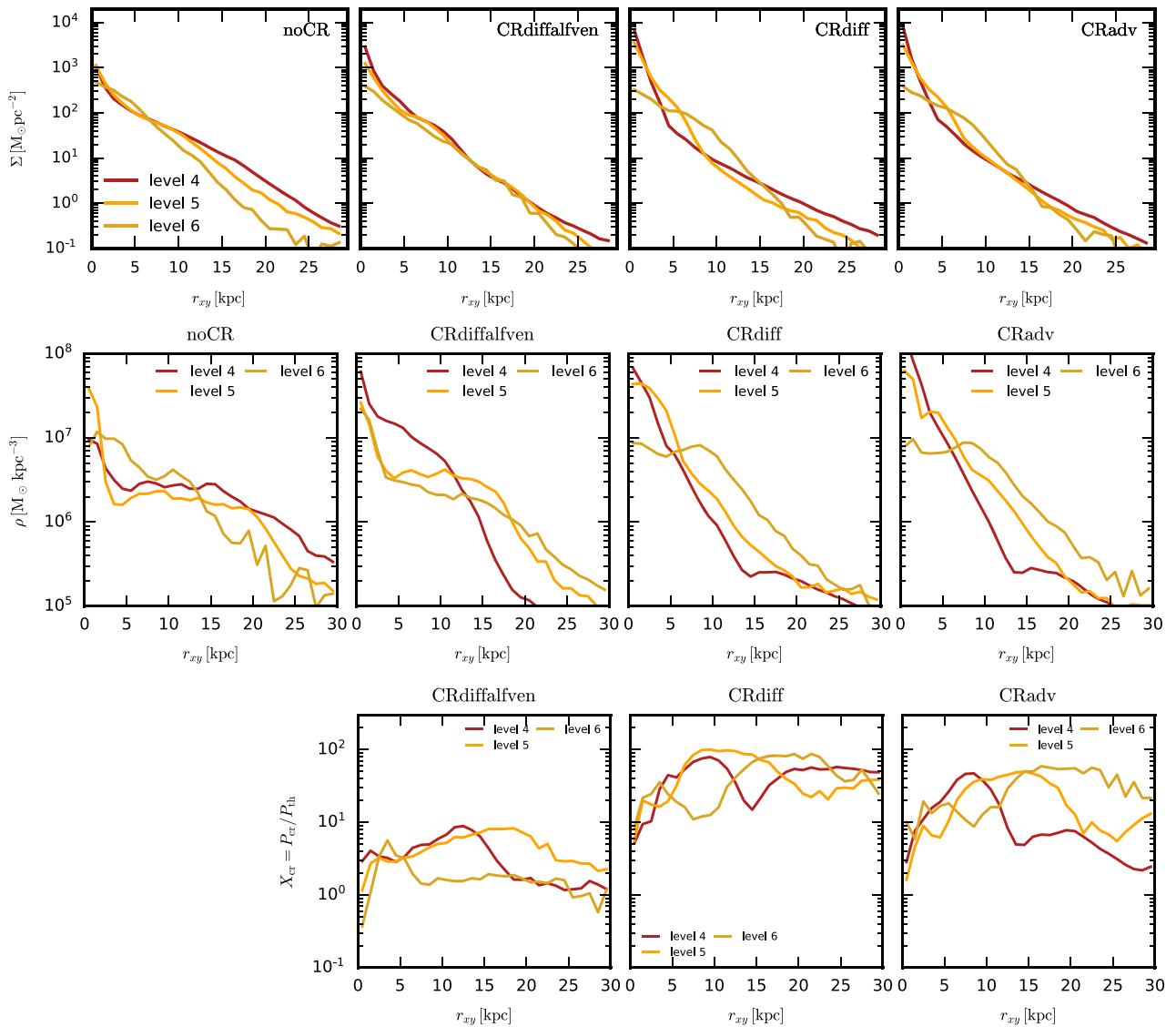

Figure D2. Comparison of the profiles of stellar surface density (upper panels), gas density (middle panels), and the CR-to-thermal pressure ratio (bottom panels) of the galaxy Au6 at three different resolution levels (as indicated in the figure legends).

Table D1. Virial mass, M_{200}, and stellar mass, M_{star} for the main galaxy across three different resolution levels for all four models.

		noCR	CRdiffalfven	CRdiff	CRadv
			Level 4		
M_{200}	$[10^{12}\,M_\odot]$	1.02	1.06	1.07	1.09
M_{star}	$[10^{10}\,M_\odot]$	4.36	5.54	5.81	6.19
			Level 5		
M_{200}	$[10^{12}\,M_\odot]$	1.03	1.02	1.07	1.06
M_{star}	$[10^{10}\,M_\odot]$	4.24	4.19	5.87	5.80
			Level 6		
M_{200}	$[10^{12}\,M_\odot]$	0.94	0.99	1.00	1.03
M_{star}	$[10^{10}\,M_\odot]$	3.78	2.84	3.44	3.71

same panels as in the upper row of Fig. 9 in the main text. The more compact and inflated gas discs in the vertical direction as well as the smoother CGM in the CRadv and CRdiff simulations are clearly visible. We find that at lower resolution (i.e. at resolution levels 5 and 6) this leads to the same hydrostatic CGM properties we have found for our fiducial resolution (level 4) in Sections 3 and 4.

We further quantify the effects of resolution on the properties of the central galaxy such as the size and morphology of the stellar and gaseous disc. To this extent we compare in Fig. D2 radial profiles of the stellar surface density (upper panels), the gas mass density (middle panels), and the ratio of CR-to-thermal pressure (bottom panels) for all three resolution levels. Stellar and gaseous disc properties are in general well converged across all resolution levels (see also Table D1). However, we note some differences of the central stellar and gas density in the lowest resolution simulations (level 6) for the CRadv and CRdiff models. For the fiducial AURIGA model, on the other hand, we see that the radial density profiles of the lowest resolution simulations results are slightly steeper. In the CRdiffalfven model the stellar surface density profile is remarkably similar across all resolution levels while the gas density profiles of level 5 and 6 slightly differ from the highest resolution level. However, we note that these differences at various resolution levels are smaller than the differences found between the two haloes studied in the main text. This argues that cosmic variance causes larger differences and that our models are sufficiently numerically converged, not only for global quantities but also for all radial profiles of interest.

Most importantly for our study is that the implementation of CR physics is converged across different resolution levels. In the bottom panel of Fig. D2 we compare the ratio of CR-to-thermal pressure across the three resolution levels and find overall good agreement between the results. The biggest differences appear for the CRadv run where the X_{cr} values at large radii are higher for level 5 and level 6 in comparison to the fiducial level 4 run.

To conclude, we find that the simulations presented here show good numerical convergence of stellar, gaseous, and CR properties across three levels of resolution. This suggests that our models are well posed to study the effects of CRs on the evolution of MW-like galaxies because the simulation properties solely depend on physical parameters and not on numerical resolution.

This paper has been typeset from a TEX/LATEX file prepared by the author.